ISTITUTO NAZIONALE DI FISICA NUCLEARE

Sezione di Milano

INFN/TC-87/11

1 Ottobre 1987

C. De Martinis and A. Ferrari:

OPTIMIZATION OF THE SHAPE OF THE HV ELETTRODE OF THE ELECTROSTATIC DEFLECTORS FOR THE MILAN SUPERCONDUCTING CYCLOTRON

Servizio Documentazione
dei Laboratori Nazionali di Frascati

Istituto Nazionale di Fisica Nucleare
Sezione di Milano

INFN/TC-87/11
1 Ottobre 1987

OPTIMIZATION OF THE SHAPE OF THE HV ELECTRODE OF THE ELECTROSTATIC DEFLECTORS FOR THE MILAN SUPERCONDUCTING CYCLOTRON

Carlo De Martinis,
Dipartimento di Fisica dell'Universita', Laboratorio Ciclotrone, Via Celoria 16, 20133 Milano

Alfredo Ferrari
Istituto Nazionale di Fisica Nucleare, Laboratorio Ciclotrone, Via Celoria 16, 20133 Milano

ABSTRACT

The electrostatic deflectors for the extraction of the beam from the Milan Superconducting Cyclotron are presently under development. The early tests[1] showed that major troubles arise from the modifications induced in the discharge mechanism by the presence of the magnetic field, resulting in a drastic reduction of the deflector performances. Therefore a detailed analysis of the electric field configuration of the deflector has been carried out in order to improve its performances. In this paper we report the results so far obtained in the optimization of the shape of the electrode and insulator fixing.

1. - INTRODUCTION

The extraction scheme of the Milan Superconducting Cyclotron[3,4] foresees two electrostatic deflectors followed by a set of 7 passive magnetic channels. A maximum electric field strength of 140 kV/cm is required for the extraction of the most energetic ions (fully stripped ions with Z/A=.5 and a maximum energy of 100 MeV/amu): with an 8 mm wide gap between the two high voltage electrodes, as dictated by the foreseen beam emittance, a maximum voltage of 112 kV is implied. These figures are not too large in comparison with the known high voltage capabilities of electrodes[5-7], but they are likely to be difficult to reach in an apparatus working in a machine with a lot of limiting constraints, such as small clearances and a very high axial magnetic field. Preliminary tests[1], carried out on a full scale prototype of the deflector, showed that the design voltage is easily reached without the magnetic field, but also showed a strong decrease in the deflector performances when a 1 T magnetic field was switched on, together with permanent damages undergone by the anode liners below and above the HV electrode.

In order to minimize the electric field on the HV electrode the behavior of different geometries has been analyzed using the code POISSON[2].

2. - VACUUM DISCHARGE MECHANISMS AND LIMITING EFFECTS OF THE MAGNETIC FIELD

An extensive exposition of the mechanisms which are believed to be responsible for vacuum discharges is not the purpose of this paper; exhaustive informations can be found in the literature[5-8]. Only some leading ideas will be reminded.

The processes that rule the vacuum discharge phenomena between metallic electrodes can be brought back to two main classes:

a)-Field emitted electrons initiated breakdowns.

b)-Micro-particle initiated breakdowns.

The first class includes all the phenomena induced by the electrons emitted by the negative voltage electrode: there are experimental and theoretical evidences that electron emission originates from sharp micro-features on the negative electrode surface, where the macroscopic electric field strength is enhanced until reaching the intensity needed for the field electron emission process (typically $> 10^9$ V/m); as a consequence,

even before reaching the breakdown voltage, a dark current is always present in a HV gap. Whenever the emission current is as large to melt for ohmic effect the emitting protrusion a plasma is created and a breakdown may occur: as the emitted current is, at given micro-protrusion features and electrode material, only function of the macroscopic surface field, this process gives place to a linear dependence of the breakdown voltage from the electrode separation. An alternative breakdown initiating mechanism, always related to field emitted electrons, occurs when the emitted electrons, accelerated to the applied voltage, melt the hit area of the anode; the breakdown voltage related to this process is not a simple function of the applied voltage and gap separation, as it depends not only on the hitting power but also on the electron beam divergence and penetration in the anode material (and obviously on the anode material thermal properties). Therefore it is not generally obvious to state which of these two processes can rule the breakdown voltage[5,7,8].

Micro-particle initiated breakdowns relate on the presence on the HV electrodes of small particles of contaminants and/or of the electrode materials which can be detached by the electric field strength when the high voltage is switched on. These particles, accelerated by the inter-electrode field, can acquire enough energy to give rise to a plasma when hitting an electrode. The breakdown voltage related to this phenomenon depends mainly on the particle acquired energy, which is a function of the applied voltage and of the micro-particle initial charge, therefore of the superficial field; then, in a very simple approximation, the breakdown voltage can be expressed by a condition like $V \cdot E \leq C$. This kind of phenomenon can become significant for a gap width larger than a few millimeters[5,7].

It is clear from these considerations that to minimize the electric field strength along the electrode surfaces is useful for all the breakdown initiating mechanisms and in particular for the ones related to field emitted electrons which shows a strong dependence on the electric field strength. Analytical formulas are available in the literature (see the Rogowski and Bruce profiles in ref. 9) for electrodes which achieve a surface electric field on the rounded edges equal or smaller than the one in the plane region. Unfortunately the clearances limitations of the cyclotron don't allow the use of such optimal configurations.

As a consequence of the early tests of the deflector prototype an extensive study was carried out to realize qualitatively and quantitatively how the magnetic field can influence the HV behavior of the deflector. Just from a preliminary analysis of the previous processes, the only one that can be enhanced by the magnetic field, in a configuration and with applied

voltages like the deflector ones, is the anode initiated breakdown related to the emitted electron heating: in fact there is no evident physical effect of the magnetic field on the micro-protrusion ohmic melting mechanism and the micro-particle trajectory modifications due to the magnetic field are quite negligible, as a straightforward calculus can show[10], resulting in micro-particle impacts with similar locations and energy deposition, with given applied voltage. This is not true for the electron trajectories which are strongly modified, undergoing a focusing process which can lead to a hitting power per unit area on the anode several order of magnitude larger than without the magnetic field[10].

These considerations make us reasonably sure that, with a strong axial magnetic field, the limiting process for our deflector performances is the anode melting induced by the cathode emitted electrons. This assertion is strongly supported by the damages induced on the anode surfaces above and below the HV negative electrode: in fact these damages look like very similar to small melted hot spots, as can be seen from fig. 2.1. Moreover a very simple calculation[10] shows that the emitted electrons can not reach the deflector septum regardless of their starting point on the cathode, but they can only travel up or down until reaching the anode liners (see fig. 4.1 and 5.1 for details about the deflector geometry): this kind of trajectories is in very good agreement with the experimental distribution of the melted spots on the liners, which resembles the shadow of the HV electrode profile, and with the evidence of no septum damages. Also the insulator performances seem to be decreased by the magnetic field: particularly insulators are often found strongly metallized and with a sharp track on a side (see fig.2.2): the first effect is likely due to the large amounts of anode material vaporized in a discharge, whilst the second can be explained by the motion of electrons emitted near the triple junction (vacuum, metal and dielectric) in the magnetic field[10].

A program was started in 1985 in order to increase the deflector performances in the magnetic field. Experimental tests has been carried out on high melting point materials as anode liners, such as Molybdenum, Tantalum and Tungsten, the use of other materials for the HV electrode, particularly Titanium, the development of new insulators, with regard both to the material and to the geometry, and the investigation of the effectiveness of a small resistor placed in the air-vacuum HV feed-through in limiting the discharge power. A summary of the first results of this program is reported elsewhere[11]. Analytical and numerical studies followed two main currents: the investigation of the motion of the field emitted electrons in the deflector[10] and the optimization of the shape of the electrode and insulator

fixing, which is discussed in this paper.

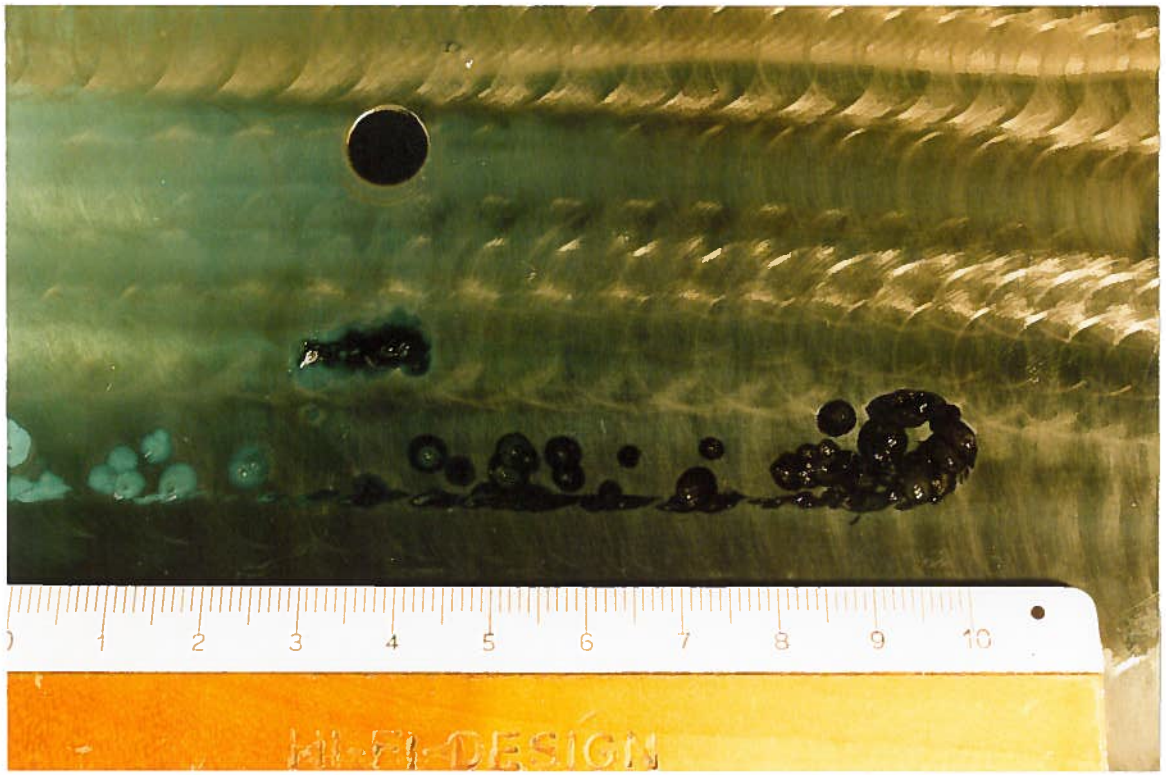

Figure 2.1: melted hot spots on a Molybdenum liner, after an extensive test in a 1 T magnetic field with voltage up to 100 kV.

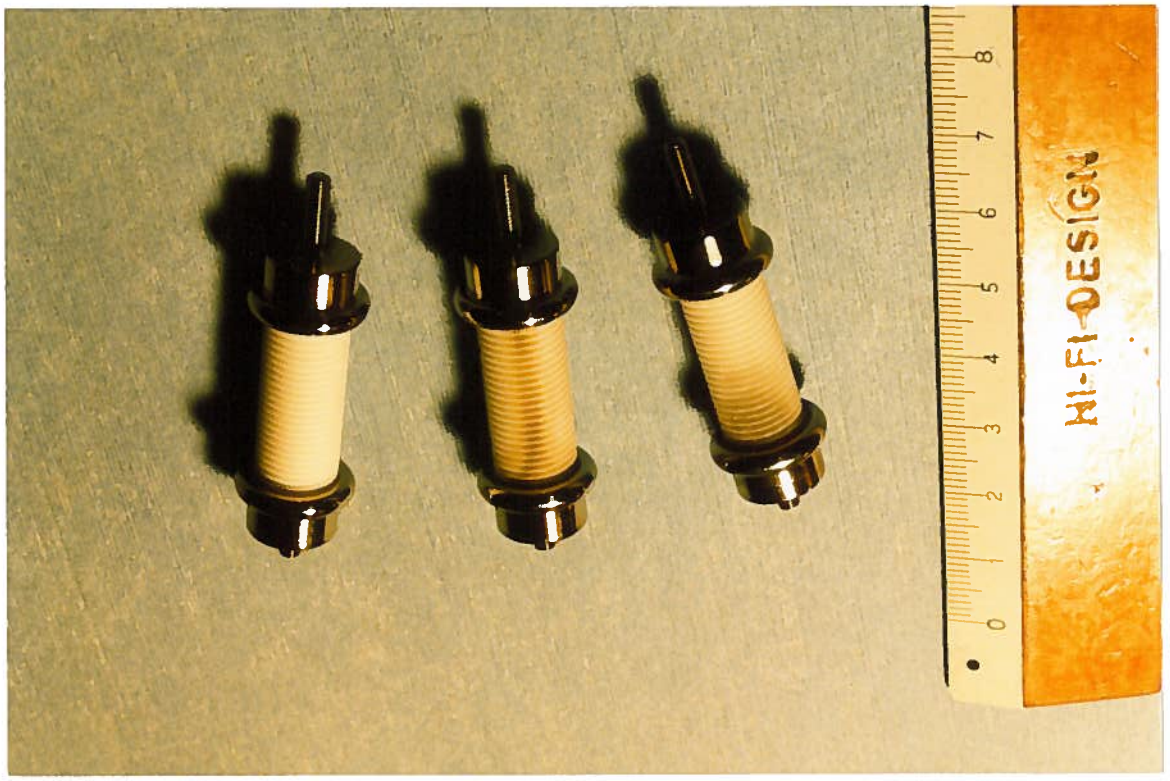

Figure 2.2: Macor insulators after extensive sparking in a 1 T magnetic field: the strong metallization and the sharp track on a side are clearly visible (the insulator on the left is a virgin one).

3. - THE USE OF POISSON FOR SURFACE ELECTRIC FIELD COMPUTATION

The POISSON[2] program package allows, besides its other options, the resolution of electrostatic two-dimensional problems on an irregular mesh, both in cartesian and cylindrical symmetry. The version we used allows a maximum of 6000 mesh points and is installed on a UNIVAC 1100 computer. A typical 5000 points problem approximately requires 20 s of CPU time for the mesh generation and 30 s for the solution convergence; further .4 s are required for every point where the potential and the fields must be computed with the fit edit option. The problem boundaries must be entered as a sequence of region and points with their logical and physical coordinates. Only vertical, horizontal and two kinds of oblique straight lines are allowed by the mesh generation code: all other lines, such as curved and generic oriented oblique lines, must be entered point per point. The boundary physical conditions can be Neumann (zero electric field flux lines) or Dirichlet conditions (fixed potential lines), dielectrics and surface and volume charges are allowed.

Before using the program for the deflector optimization some tests were carried out in order to investigate the code performances in electric field computation with particular care for points very near to the problem boundaries. Two main tests were carried out: two fixed potential coaxial cylinders for the cartesian coordinates, and two concentric spheres for the cylindrical ones: the logical and physical meshes and the equipotential lines of these tests are presented in fig. 3.1.1-3.1.4 and fig. 3.2.1-3.2.4. Despite these very simple geometries, these tests are believed to be significant as no particular symmetry is present in the meshes and no symmetry condition was given to the program when using the field editing option (excepted for the mid-plane even symmetry in the cartesian test, as discussed later); moreover these kinds of curved surfaces are very similar to the ones we want to investigate for the electrode (see for comparison fig. 3.6).

3.1 - Cartesian symmetry

The final results of the cartesian test are quite remarkable: the accuracy of the field computed with the logical and physical meshes showed in fig. 3.1.1-3.1.3, is plotted in fig. 3.3 for four radii close to the internal one, for the mean radius and for four radii near the external one. The field computed at the mean radius are accurate within few parts over ten thousand and even the fields computed near the boundaries seem very accurate (within .1%). This result was not easily got: two main problems had to be overcome.

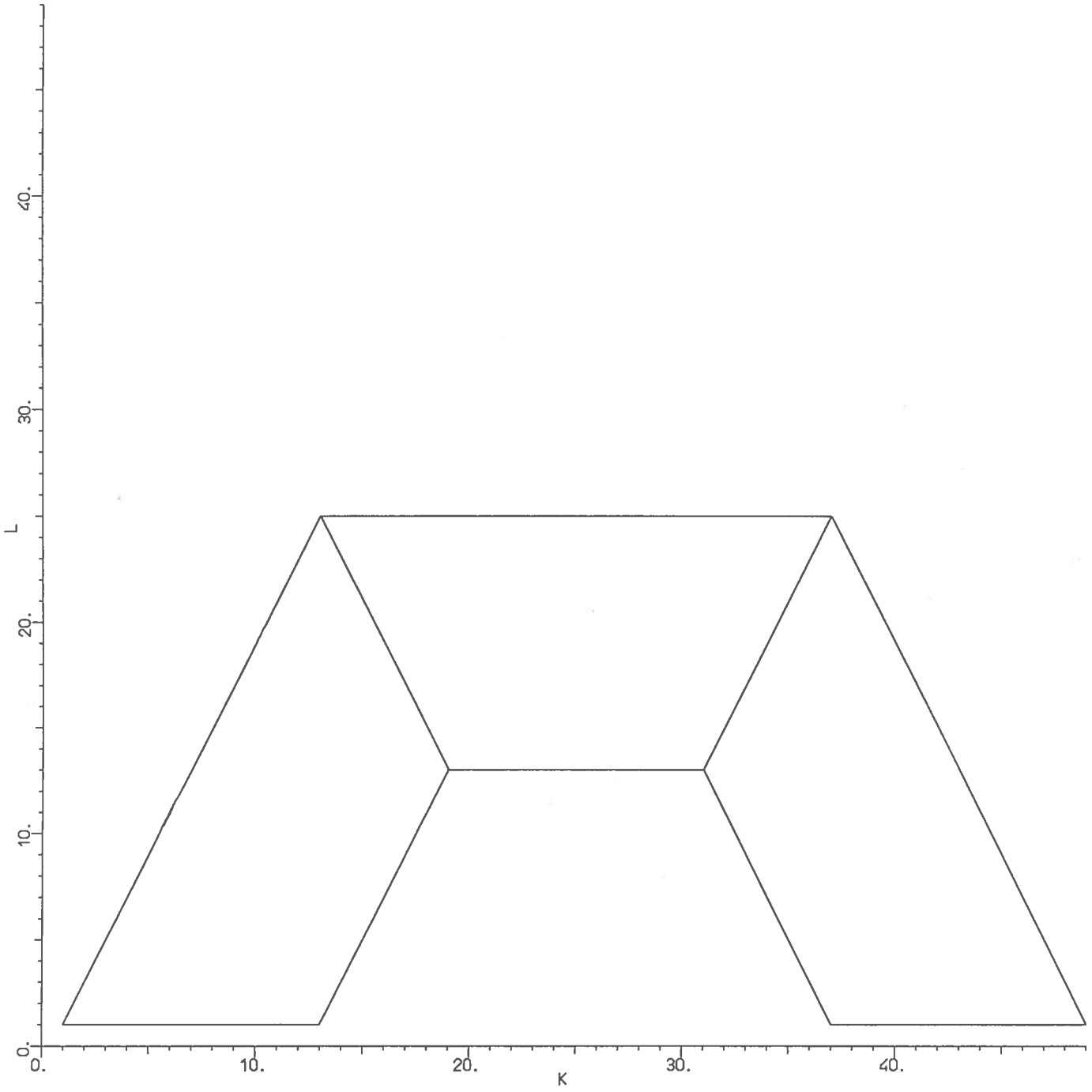

Figure 3.1.1: logical mesh for the coaxial test, the lines inside the gap are added to regularize the physical mesh.

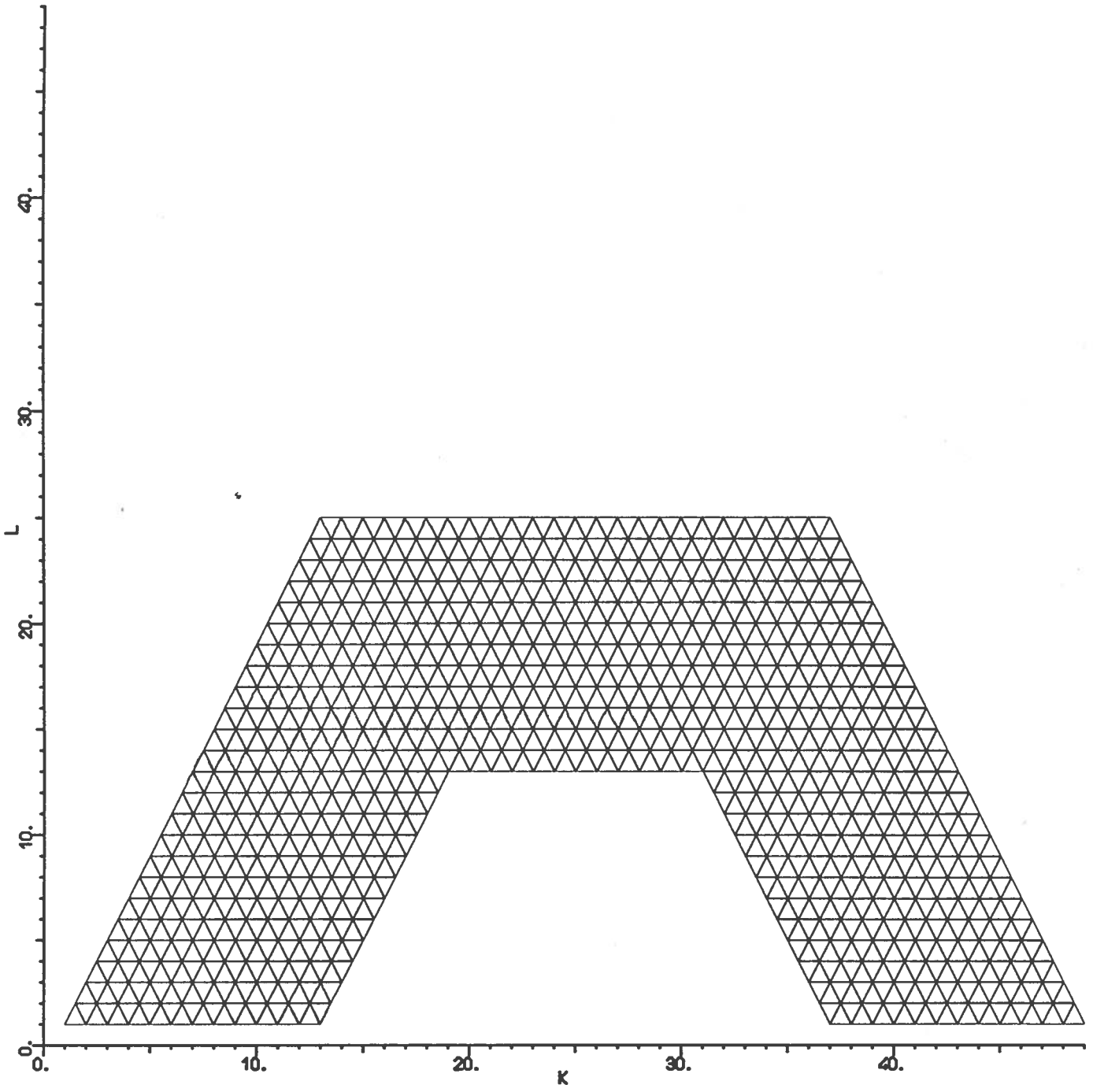

Figure 3.1.2: logical mesh for the coaxial, with triangles.

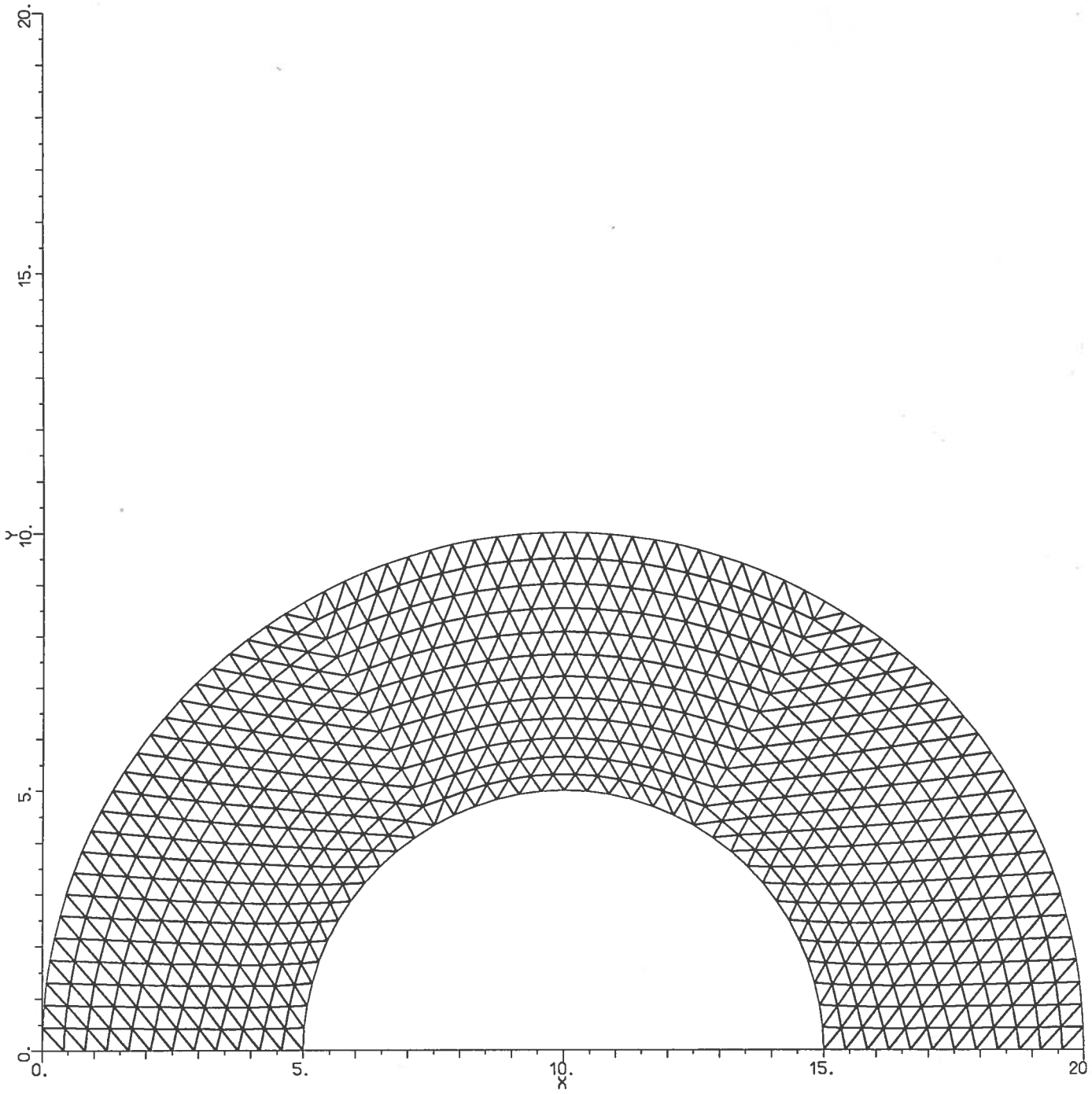

Figure 3.1.3: physical mesh for the coaxial, with triangles.

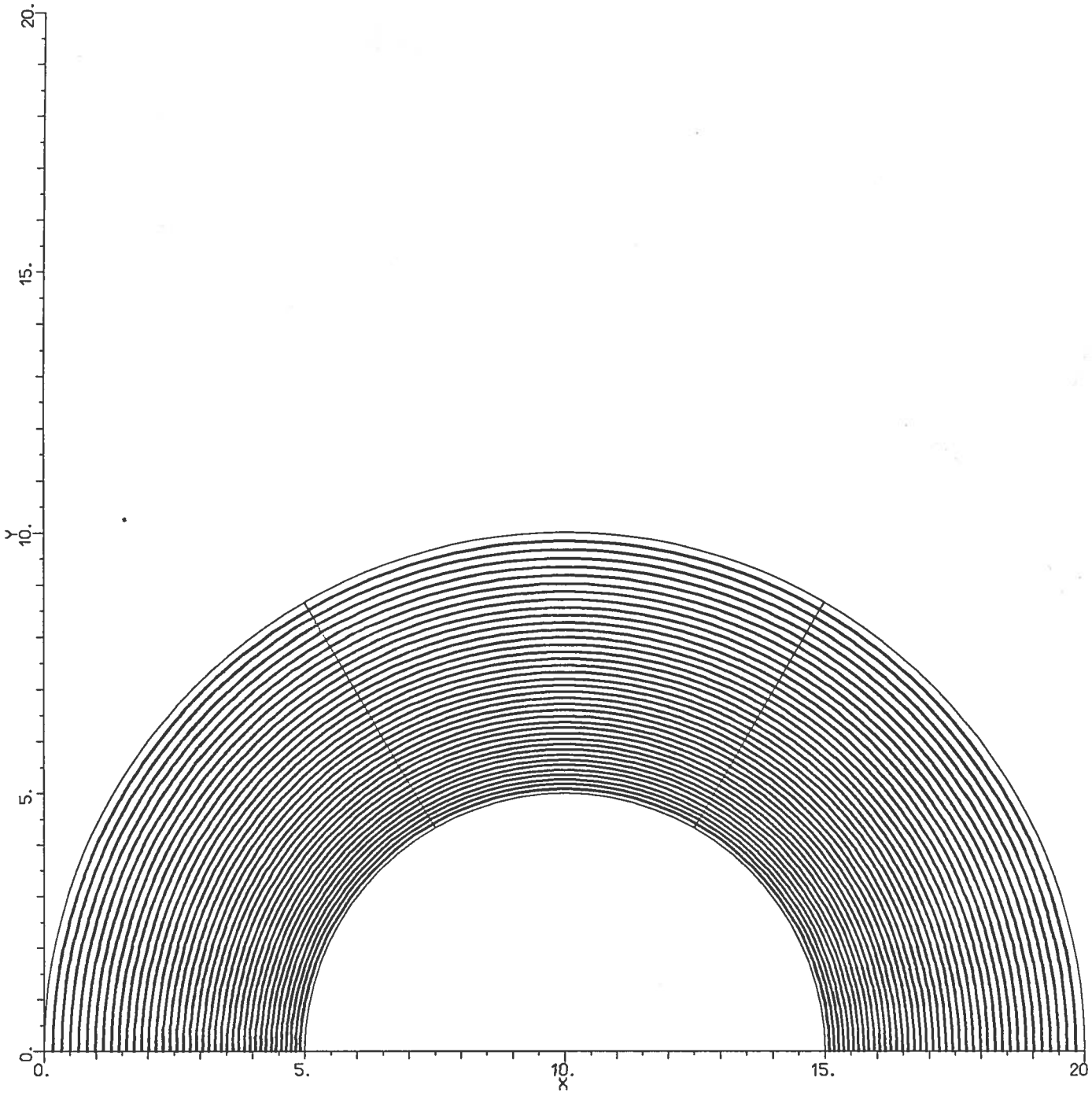

Figure 3.1.4: equipotential lines for the coaxial, plotted every 2.5% of the applied voltage.

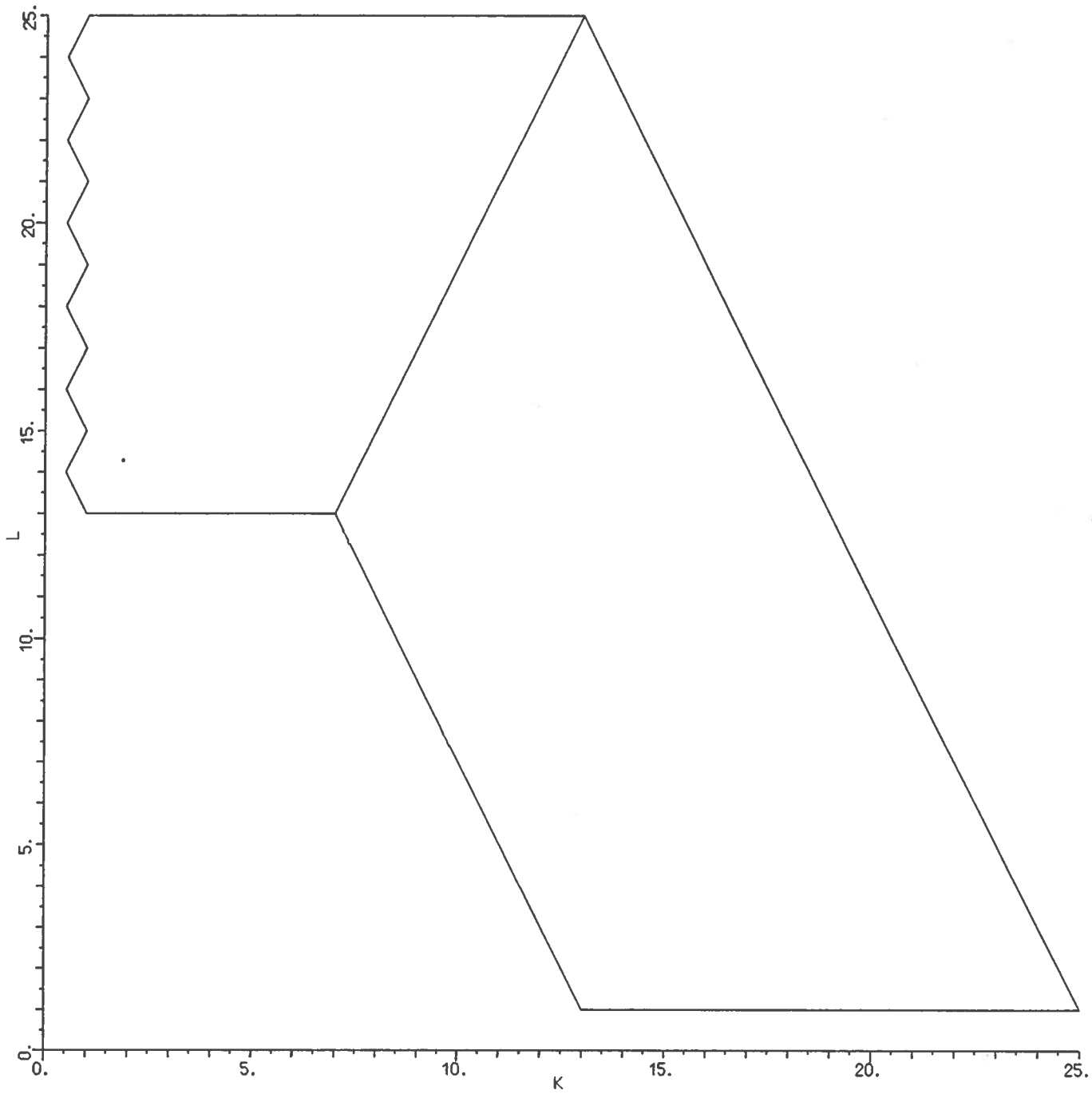

Figure 3.2.1: logical mesh for the concentric spheres test, the line inside the gap is added to regularize the physical mesh.

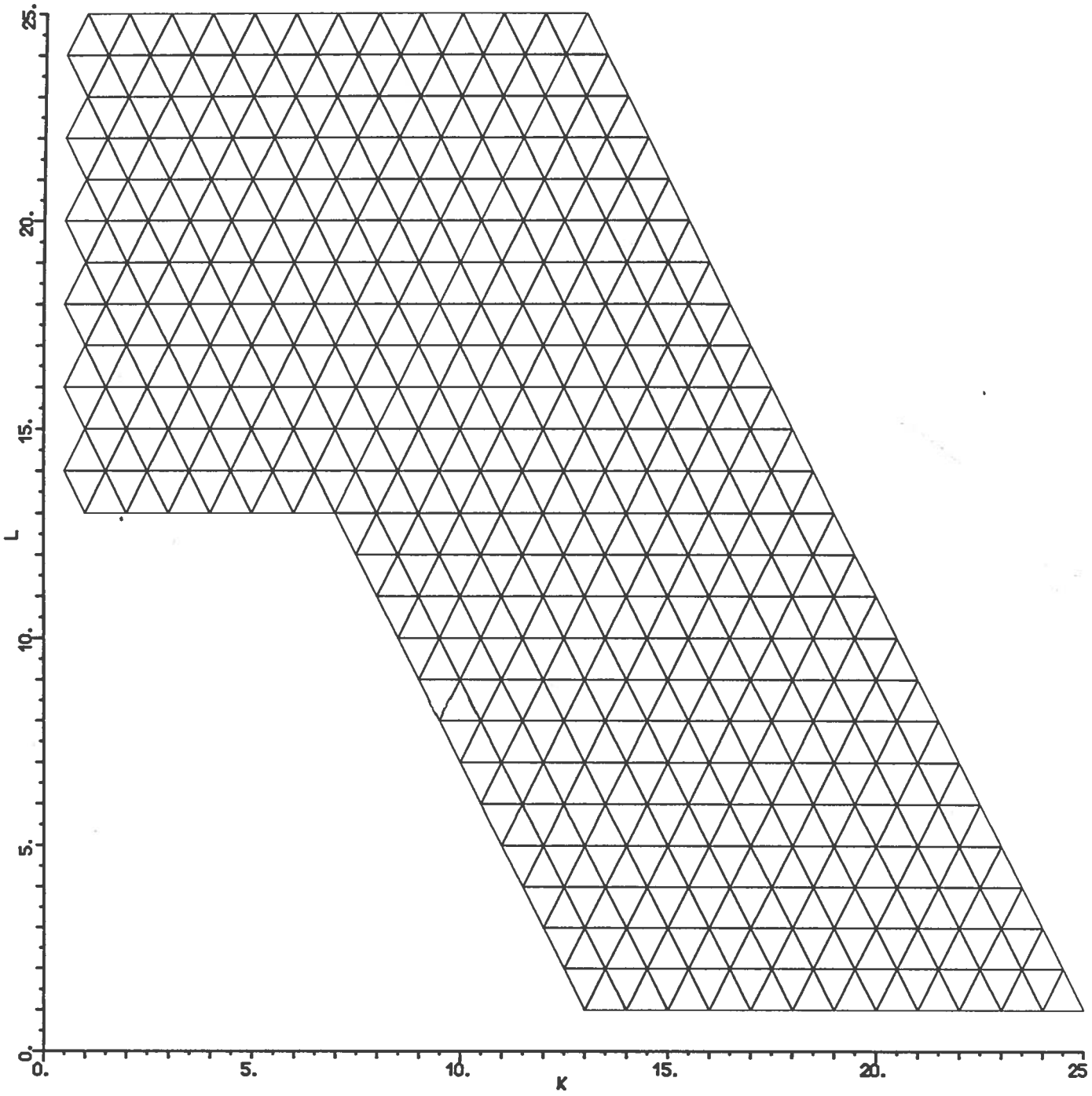

Figure 3.2.2: logical mesh for the spheres, with triangles.

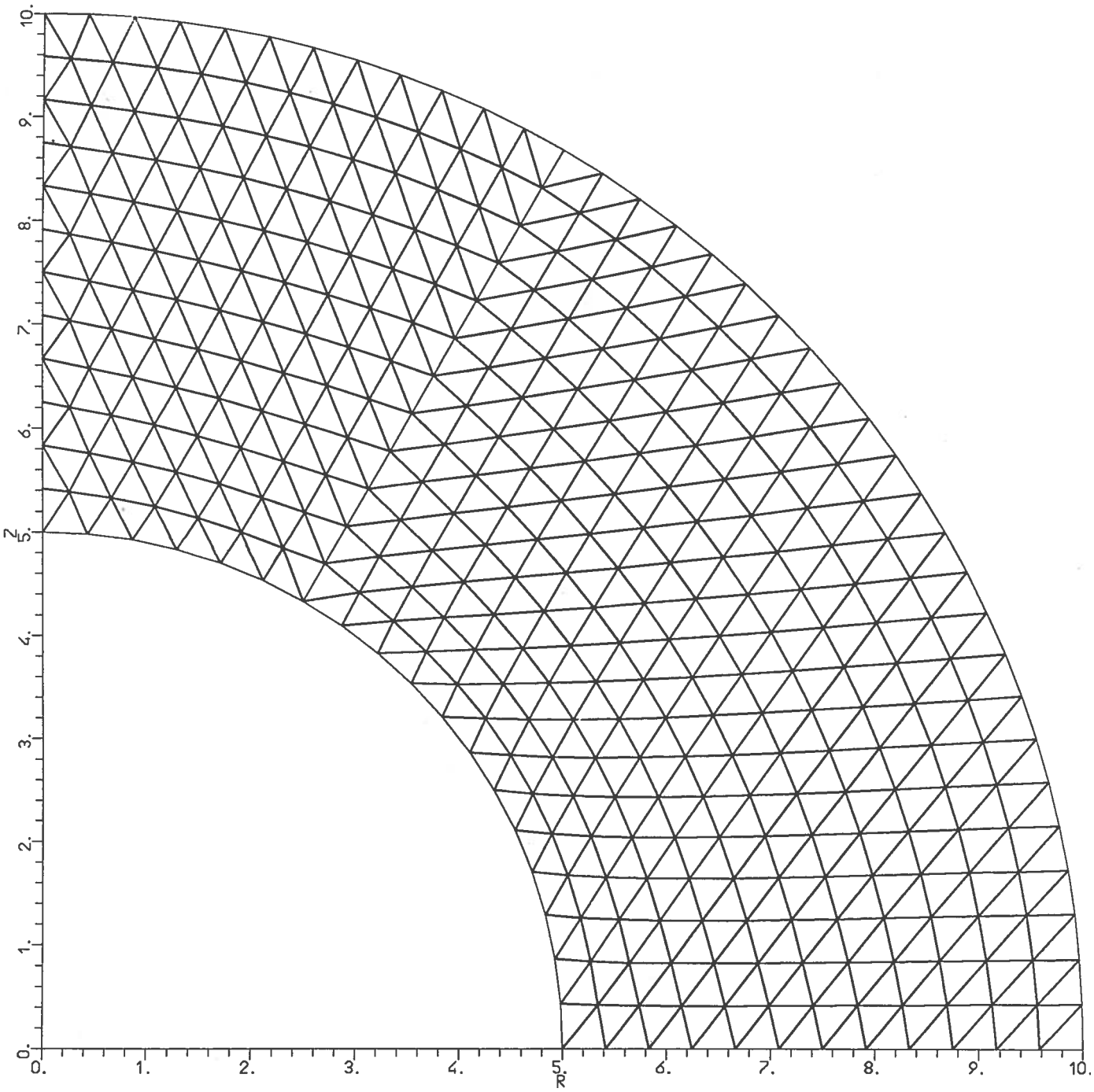

Figure 3.2.3: physical mesh for the spheres, with triangles.

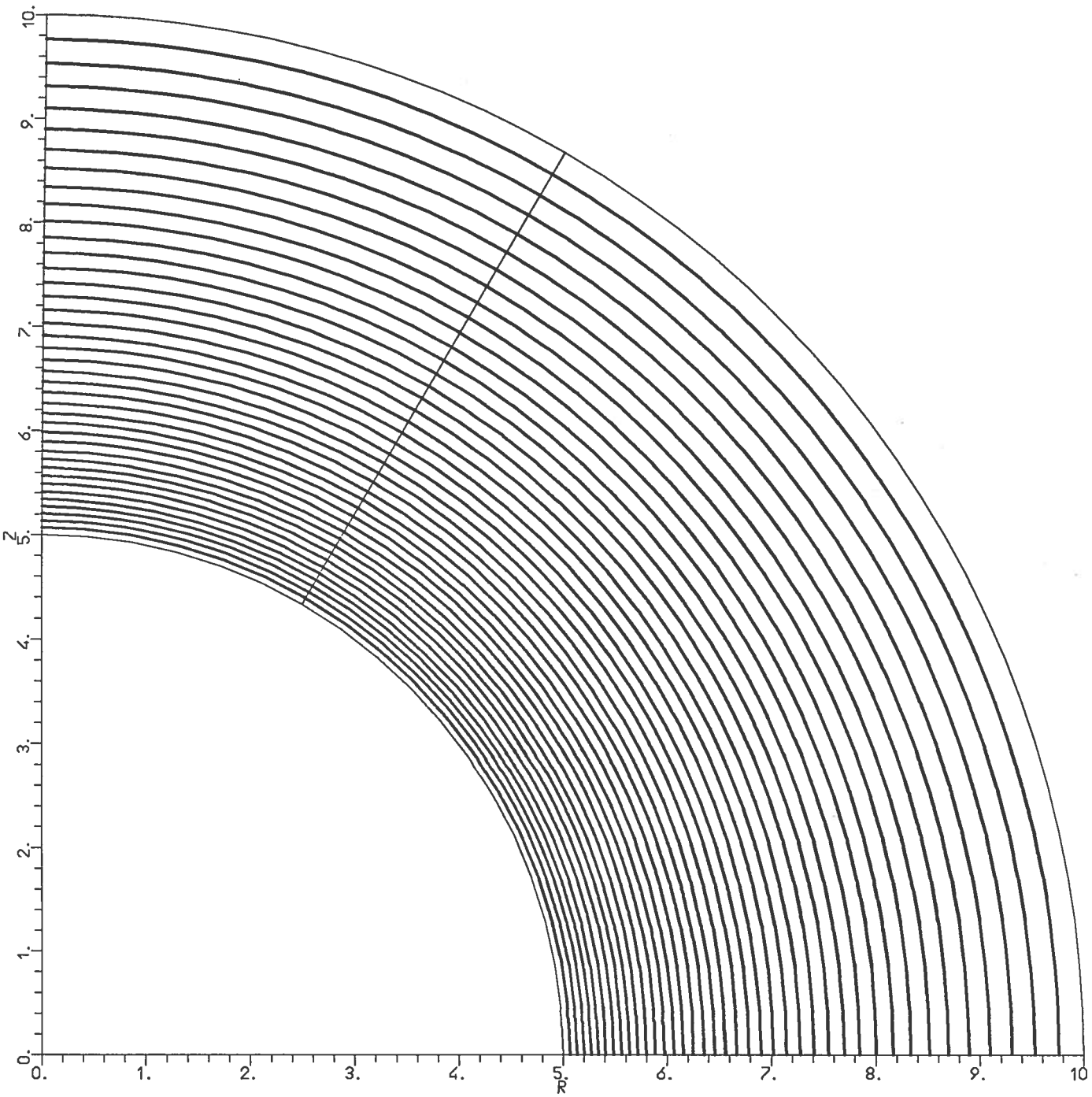

Figure 3.2.4: equipotential lines for the spheres, plotted every 2.5% of the applied voltage.

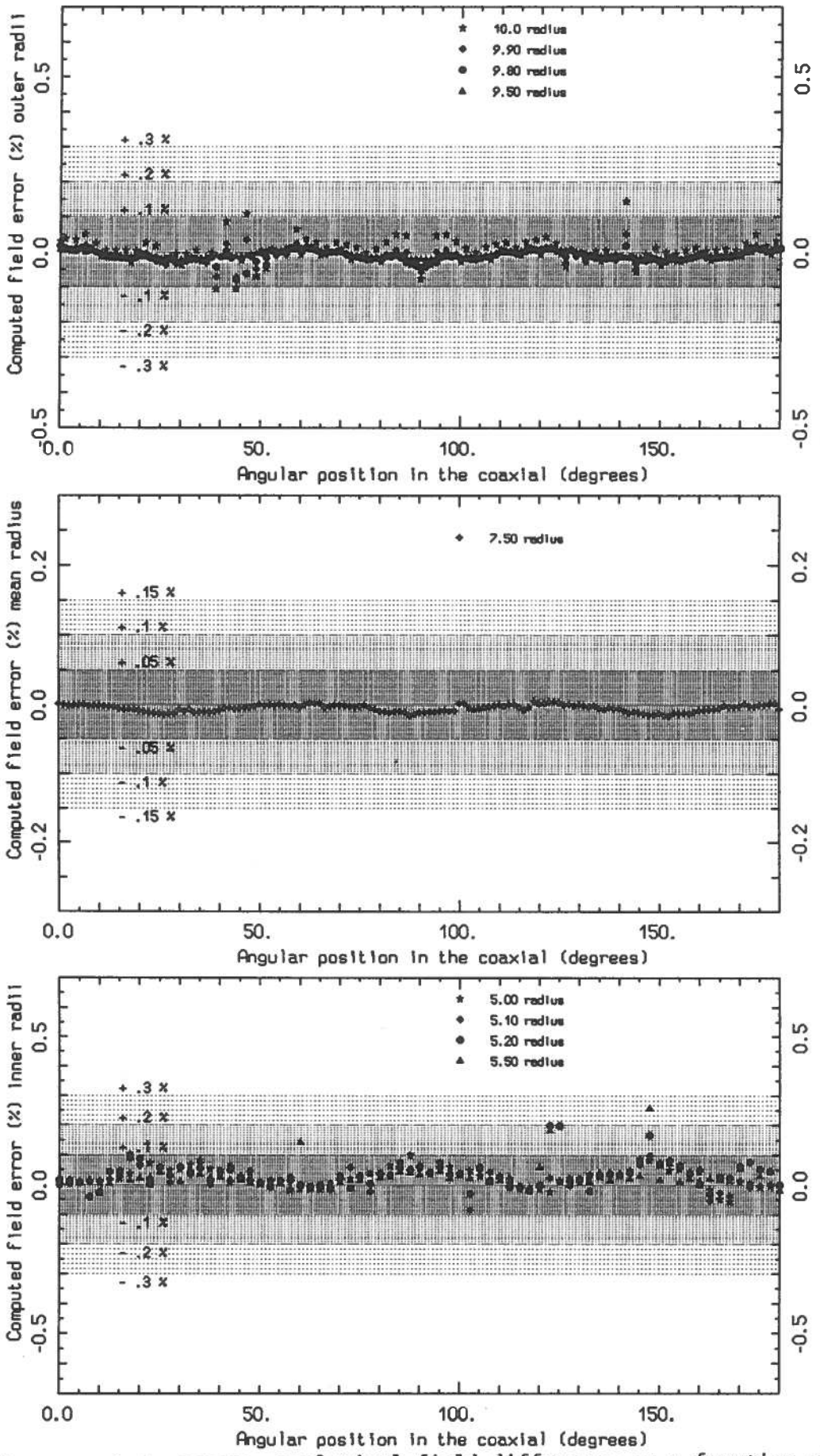

Figure 3.3: computed versus analytical field difference as a function of the angular position (angles counted anti-clockwise) in the coaxial (R_{min}=5, R_{max}=10), for various radii.

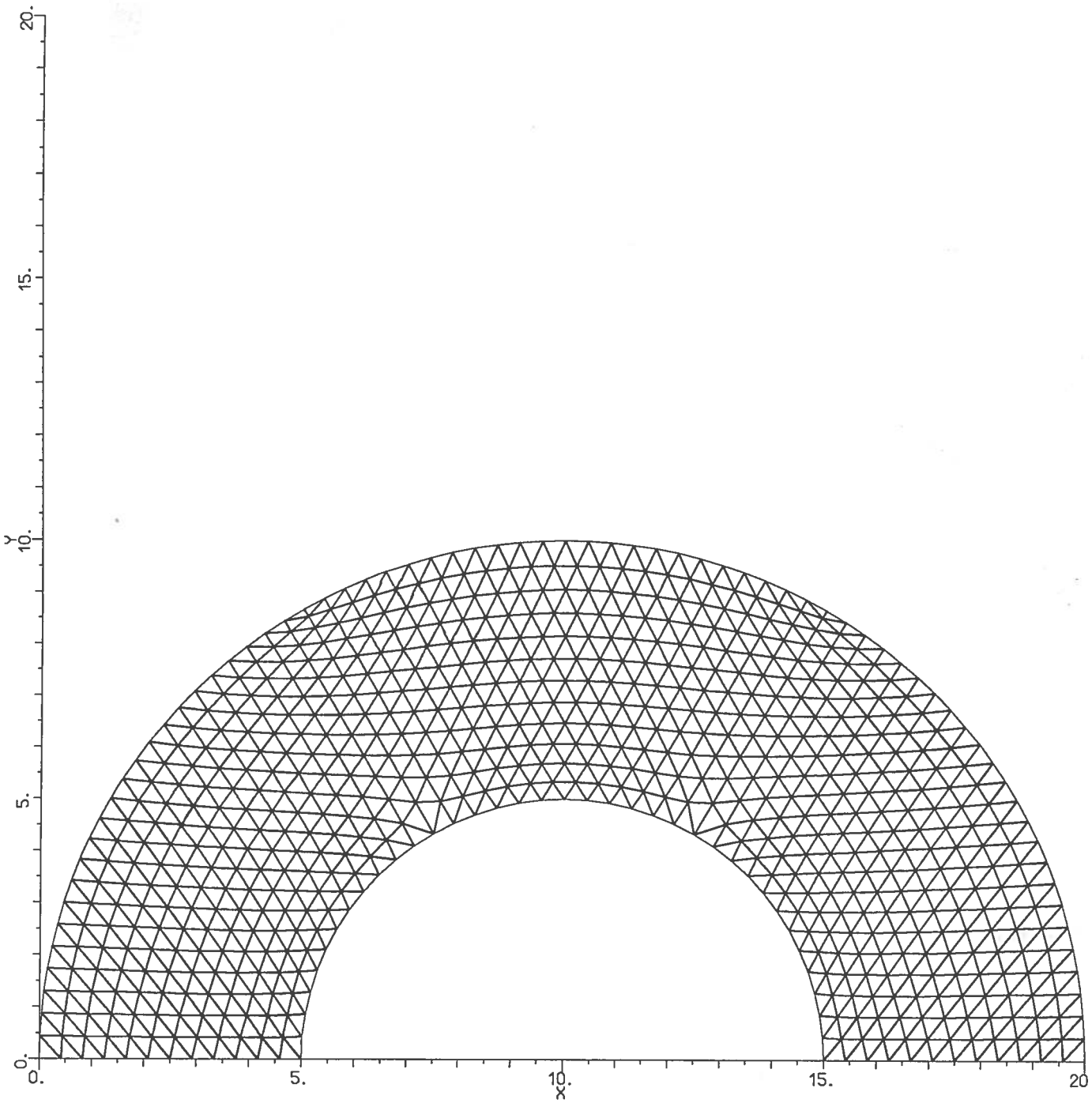

Figure 3.4: physical mesh for the coaxial, without regularizing lines.

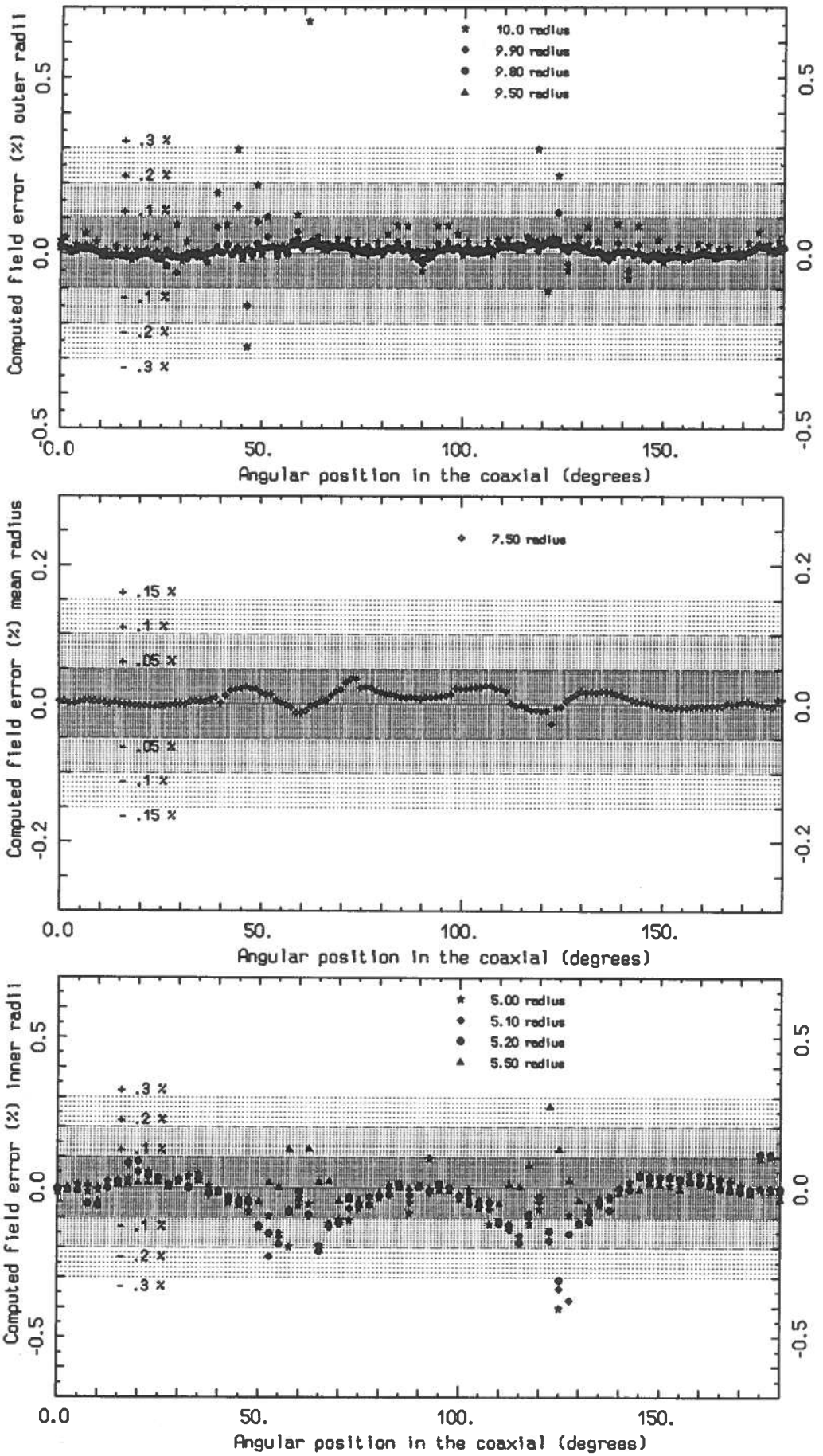

Figure 3.5: computed versus analytical field difference as a function of the angular position (angles counted anti-clockwise) in the coaxial (R_{min}=5, R_{max}=10), for various radii, for the mesh of fig. 3.4.

The former related to the parameters used in the POISSON field edit option: the default parameters works quite badly near the boundaries as they often give results thoroughly wrong for the field modulus, direction and trend. The problem can be easily overcome if the weight parameter of the first neighborhood points in the fit process is switched to a non-zero value (typically to a value equal to the weight of the second neighborhood): with this choice the fit option works rather well, is not very sensitive to the other parameters and gives far from the boundaries results very similar to the default choice. This trouble is likely to be due to the lack of usable points near a boundary: if the use of the first neighborhood points is inhibited probably the harmonic function used for the fit process can "over-fit" the few points used, resulting in oscillatory behaviors which are physically inconsistent. The mid-plane even symmetry condition has always been used for our cartesian coordinates problems (obviously they are really symmetric with respect to the mid-plane!) as it gives a further little improvement in the results without troubles near the boundaries.

The latter problem related to the better way of modeling a circumference when using the logical coordinates. The first idea was to assign to the circumference the closest points of a regular mesh, but it worked rather badly as the resulting fields were somewhat irregular; after several attempts it was recognized that the better results are got with logical meshes which use hexagonal lines to describe circumferences. With this kind of meshes one must be careful only to the corners in the logical lines (for a semi-circumference the points at 60° and 120°), but also these points can be easily regularized. The field computed with a little less regular mesh (showed in fig. 3.4) than the one of fig. 3.1.3, are plotted in fig. 3.5: the little "bumps" in the field error around 60° and 120° are clearly visible, specially for the radii closer to the boundaries. In problems with a more complex geometry the error introduced by a missing or insufficient regularization of such points can be enhanced: for example two meshes, which differ only for the regularization of these points, are shown in fig. 3.6 and 3.7 (the two meshes refer to the deflector geometry G3, see chapter 5. for details). The distortions in the not regularized grid causes the computed fields to show a worse regularity: in fig. 3.8 the error percentage in the fields on the semi-circumference and at two slightly larger radii are plotted. The reference value is the average of the field at the inner radius and of the field at the two larger radii extrapolated to the inner one with a 1/r law, that is expected to be true at radii very close to the electrode surface: this representation is a self-consistency test which gives interesting indications on the accuracy of the computed fields. A comparison of the two plots of fig.

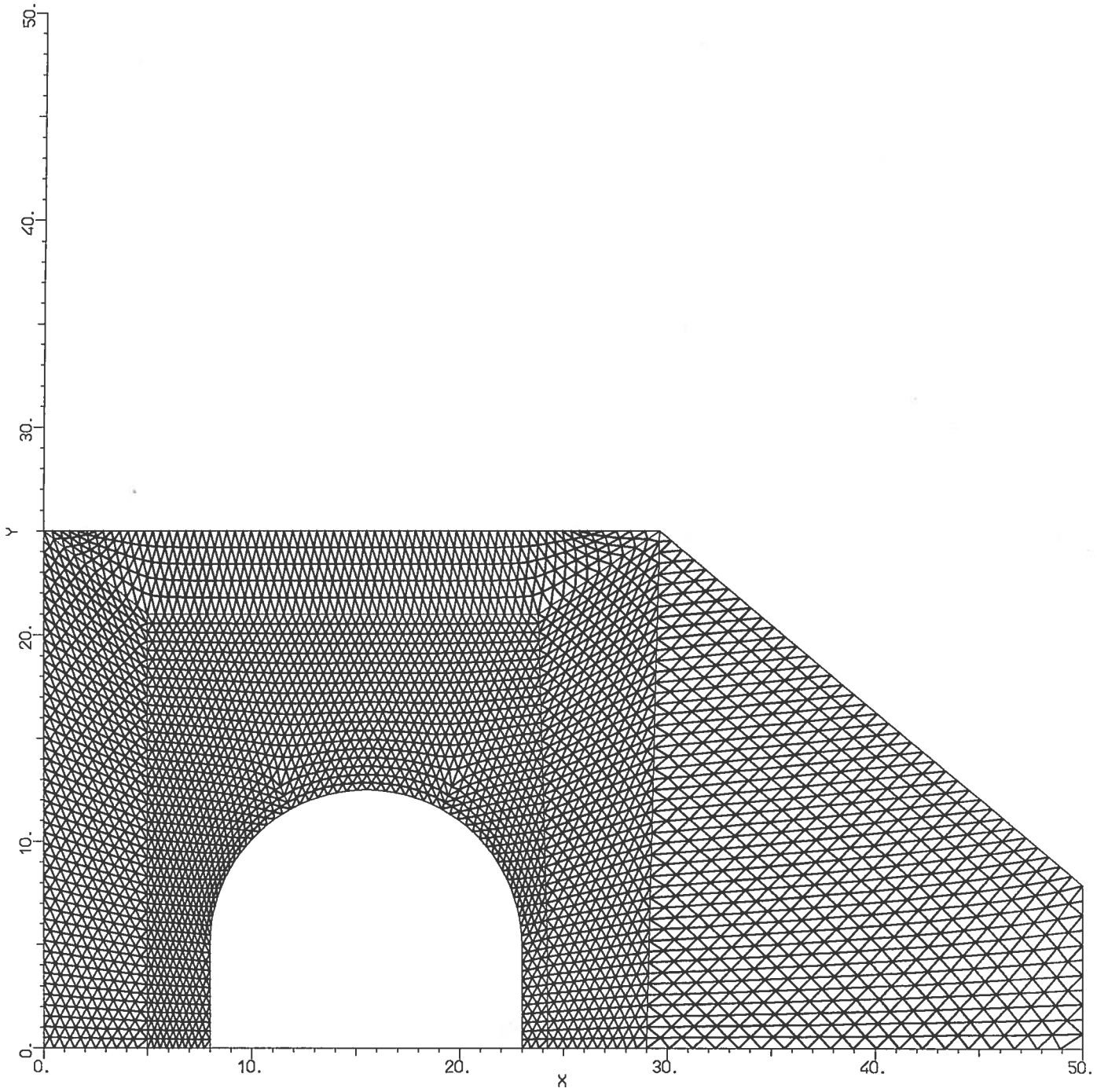

Figure 3.6: physical mesh for the deflector geometry G3 (see chapter 5), with a costant electrode radius of 7.5 mm. Note the different density of mesh points, studied to have good results in the electrode area, which is obviously the area with the largest gradients, without exceeding the maximum number of mesh points allowed.

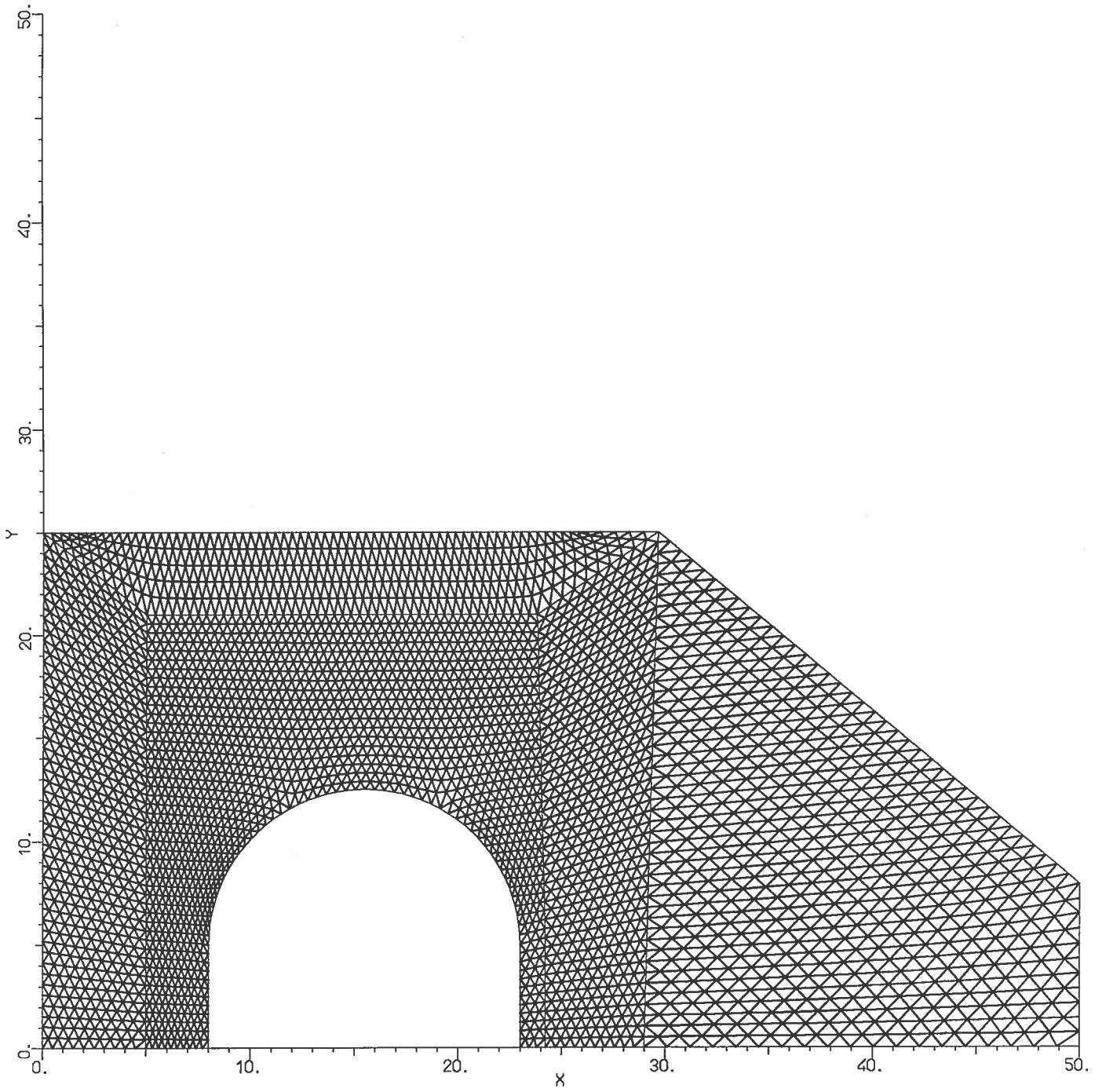

Figure 3.7: the same physical situation as in fig. 3.6 but with the mesh triangles near 60° and 120° on the electrode curvature not regularized.

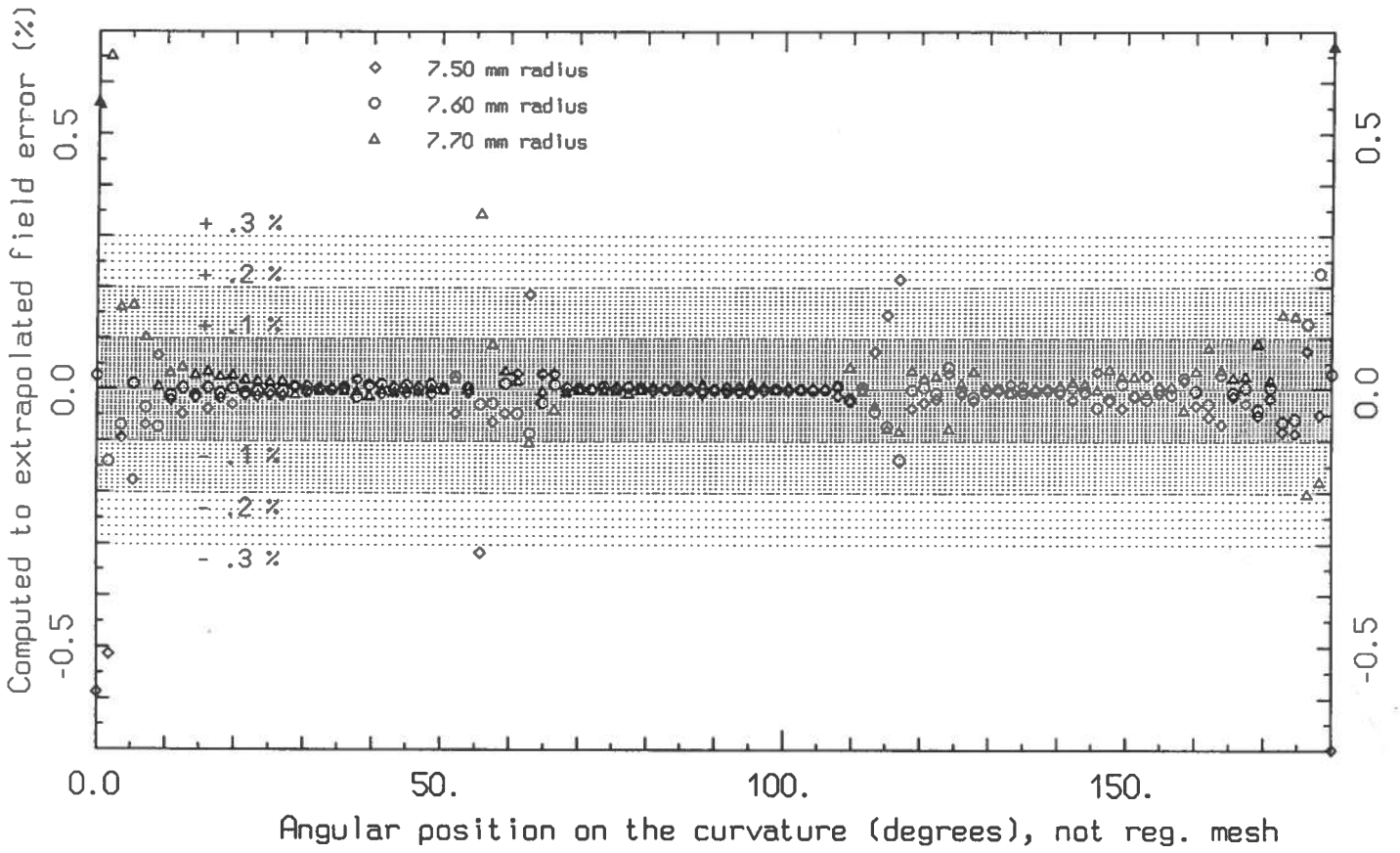

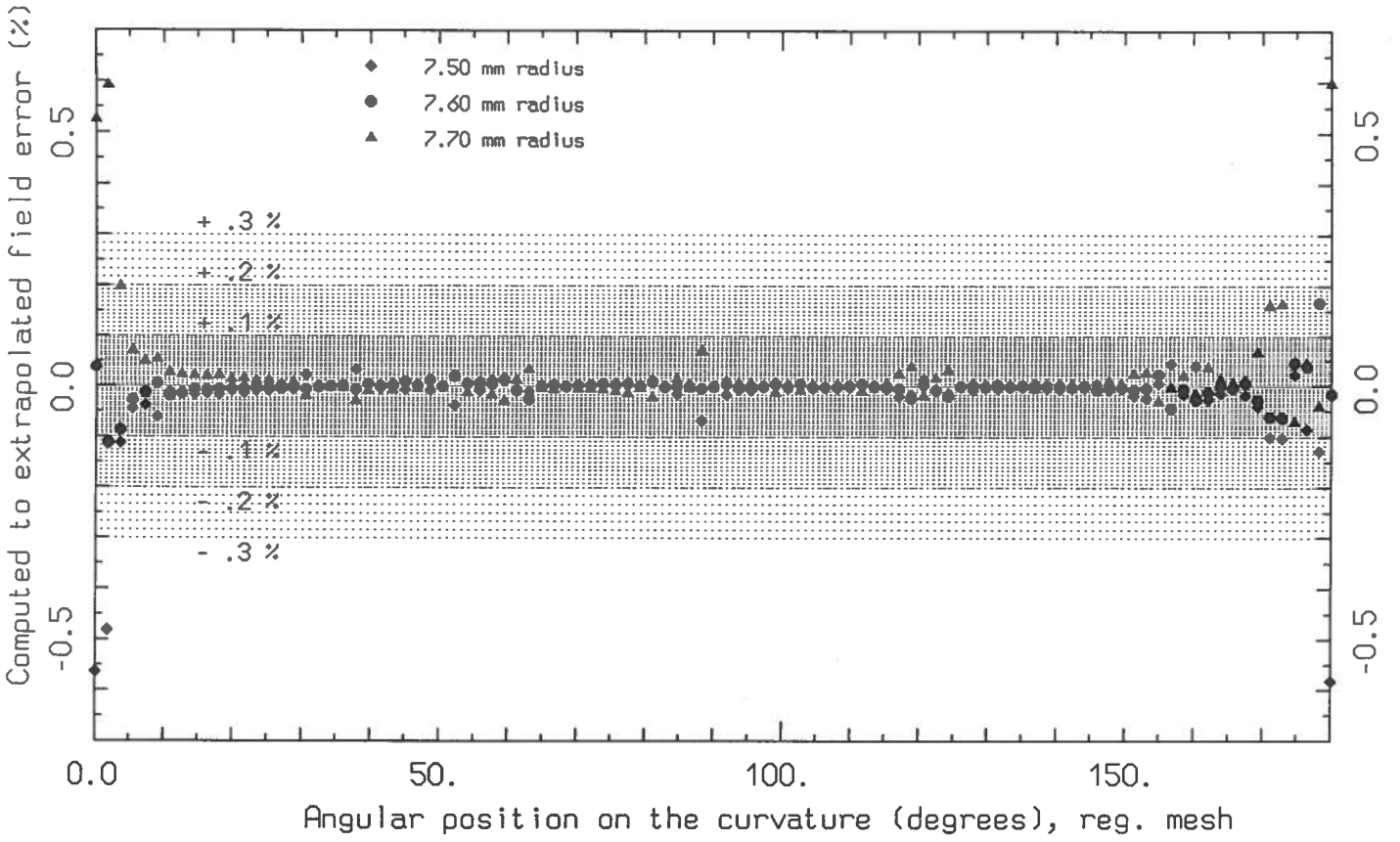

Figure 3.8: accuracy and self-consistency test (see text for explanations) for the fields computed with a regularized mesh (fig. 3.6) and a not regularized one (fig.3.7) (angles counted clockwise).

3.8 shows the "noise" in the not regularized grid near 60° and 120° (the noise at 0° and 180° is real, as the semi-circumference is terminated on two straight sections): a further confirmation is given in fig. 3.9 where the percentage difference in the computed fields and in the extrapolated mean fields between the two meshes is plotted. The physical mesh of fig. 3.6 is also an example of how to distribute the mesh points (the maximum allowed number for our POISSON version is 6000) in the problem in order to have a better resolution in the area of greater interest (e.g. the HV electrode) and of larger potential variation. These considerations enlighten that cartesian

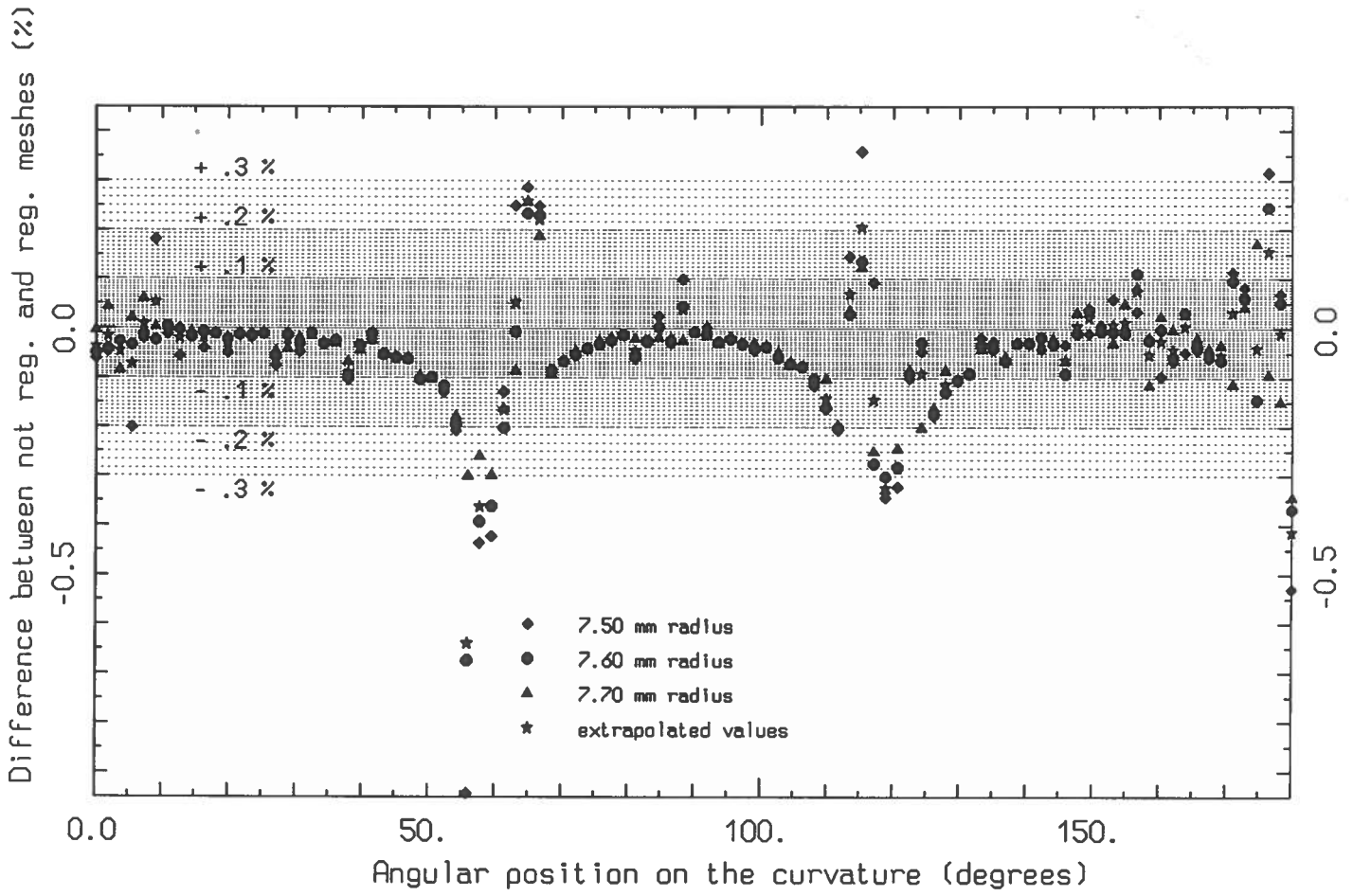

Figure 3.9: differences in the computed field between the two meshes showed in fig. 3.6 and 3.7 (see text for details).

problems with grid patch on curved surface of a few degrees (5° in the fig. 3.1.3 mesh, but 10° grid step were also tested still giving small errors, <1%) can be studied with a good precision even near the boundaries, and that an estimated error of few per cents is likely to be conservative.

3.2 - Cylindrical symmetry

The results of the test carried out on the mesh of fig.3.2.3, which represents two concentric spheres at fixed potentials, are plotted in fig. 3.10: a comparison with fig. 3.3 shows the worse accuracy achieved in the computed fields. However the error on the computed fields is still small (<.5%), except for the points near 90° and 0°. This is easily explainable when considering that the fields are computed without any symmetry condition given to the fit (so the errors near 0° depends on the lacking mid-plane symmetry) and that the points near the r=0 axis (90°) are very critical in the fitting process. All the considerations developed for the cartesian coordinates about the mesh topology and the fit parameters are still valid excepted for the mid-plane symmetry condition which gives near the boundaries some points with field markedly wrong (up to 40%): however it is often necessary to use various combinations of weights before finding the one which works well on all the surface. Moreover the combinations with a first weight different from zero are not so good far from the boundaries as the default one. A possible explanation of the worse results of the concentric spheres could be found in the larger potential gradients with respect to the coaxial: one could think that the grid step is adequate for the potential variations of the coaxial but too large for the steeper variations of the sphere. So another test, very similar to the one showed in fig. 3.8.1, was carried out using the same mesh of fig. 3.6 but in cylindrical coordinates with the X coordinate substituted by the R coordinate ranging from a minimum radius of 750 to a maximum of 800 (the mesh is showed in fig. 3.11). As the electrode gaps are much smaller of these radii, no large difference is expected in the computed field with respect to the one of the cartesian situation. In fig. 3.12.1 the computed fields are plotted in the same way of fig. 3.8.1, while in fig. 3.12.2 the difference between the fields of the cylindrical and cartesian meshes are plotted. Two major considerations arise from these plots: first, despite the very similar fields, the cylindrical solution seems intrinsically less precise than the cartesian one; second, the differences between the curved problem and the straight one are very small if the curvature radius is much larger than the electrode gap. It should be noted that these differences have the sign one can expect considering the electrode gaps as cylindrical coronas.

We may conclude that, for geometries like the deflector ones, the computed fields are likely to be precise within few per cents, both in cartesian and cylindrical coordinates, provided all the tricks and controls previously described are performed. However cartesian problems are more precise and easier to study: as the deflector curvature will be of the order

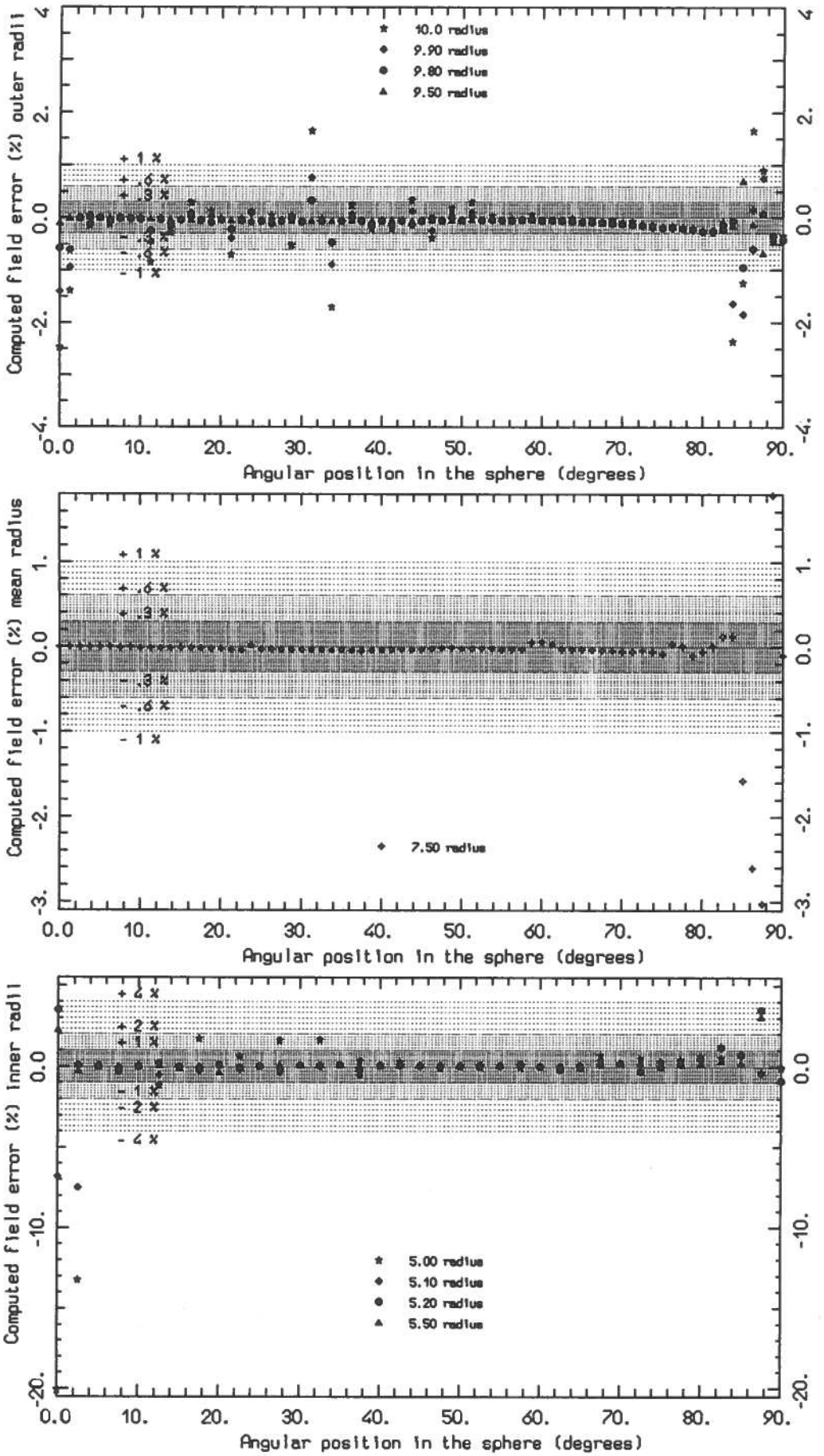

Figure 3.10: computed versus analytical field difference as a function of the angular position (angles counted anti-clockwise) in the spheres (R_{int}=5, R_{ext}=10), for various radii.

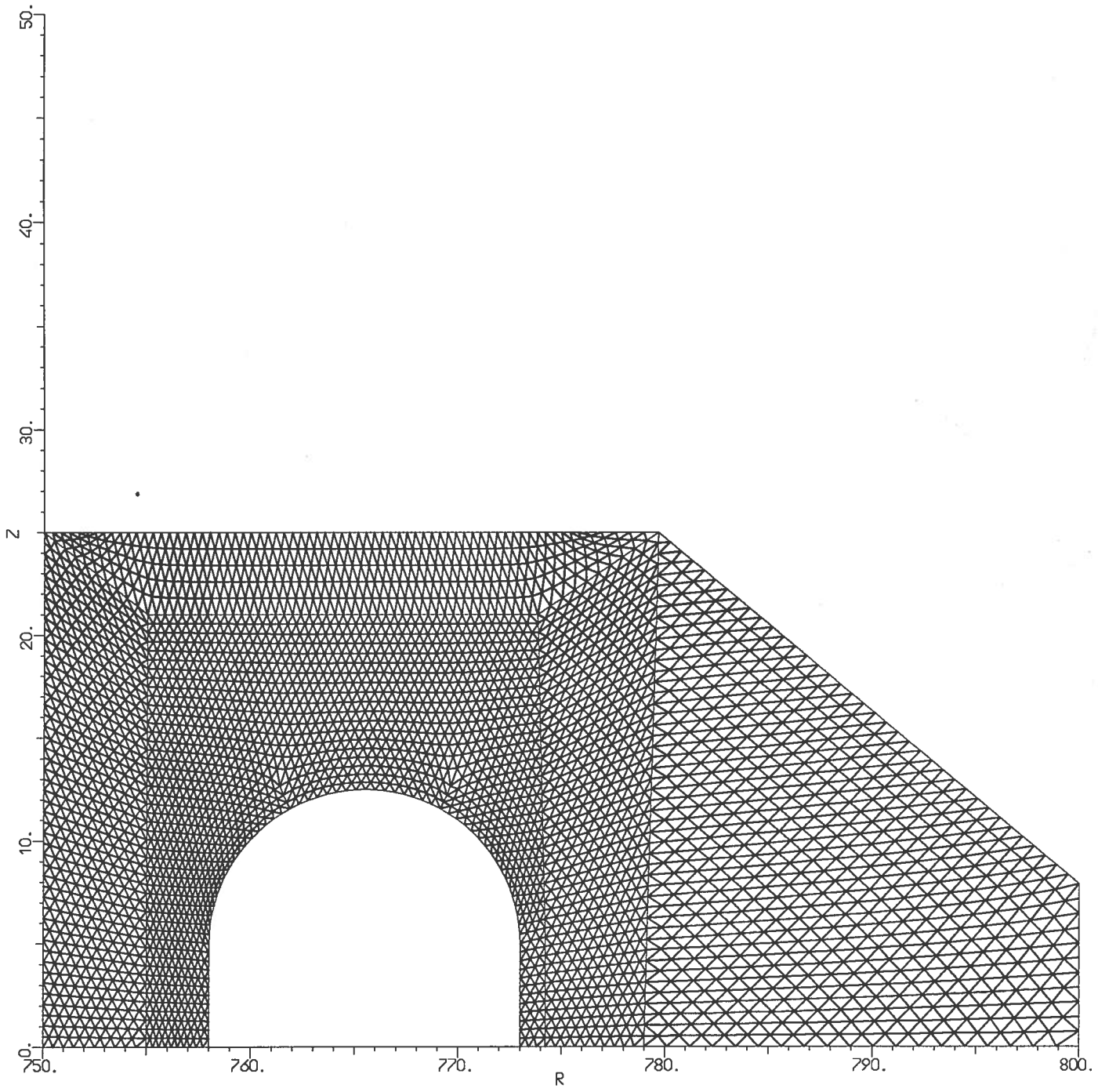

Figure 3.11: physical mesh for the deflector geometry G3, like fig. 3.6, but for a curved deflector (curvature radius at the septum 750 mm, like the real one).

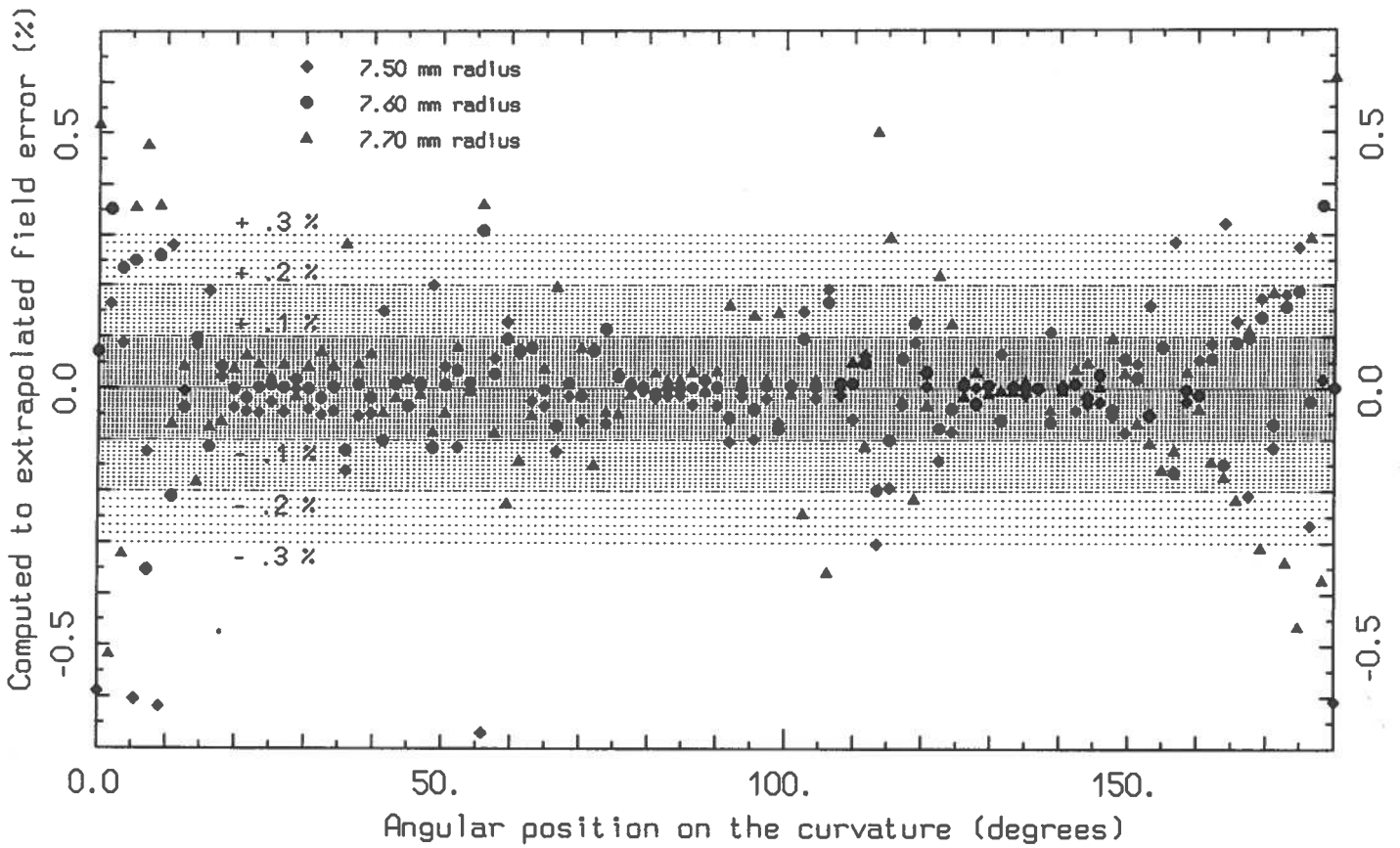

Figure 3.12.1: accuracy and self-consistency test for the curved mesh of fig. 3.11 (angles counted clockwise).

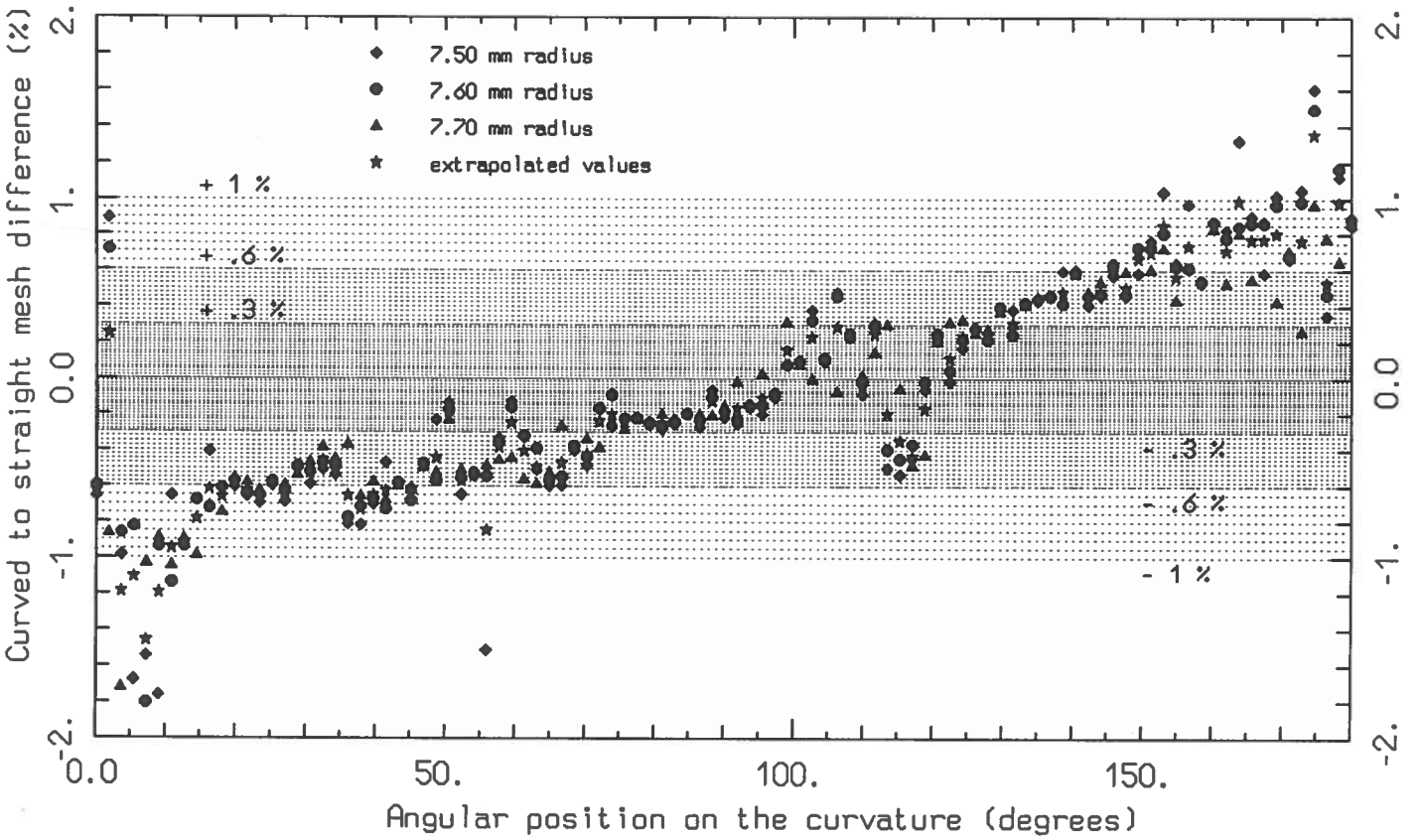

Figure 3.12.2: differences between the fields of the straight (fig. 3.6) and the curved mesh (fig. 3.11) for the deflector geometry G3.

of 750 mm for the first deflector and even larger for the second, while the electrode gap is 8 mm wide, all the deflector geometries have been studied in cartesian coordinates. The error we made is small, as fig. 3.12.2 shows, and moreover the most of the experimental tests were and will be carried out for simplicity with a straight (and shorter) prototype.

4. - CALCULATIONS RELATIVE TO THE EARLY GEOMETRY

Before trying to improve the electrode geometry, electric field calculations were made on the deflector prototype in order to get the starting results; a description of all the features of the codes and of the grids we used and of the result reliability is given in the previous chapter. In fig. 4.1 two sections of the old deflector prototype are shown; a generic section and one along an insulator.

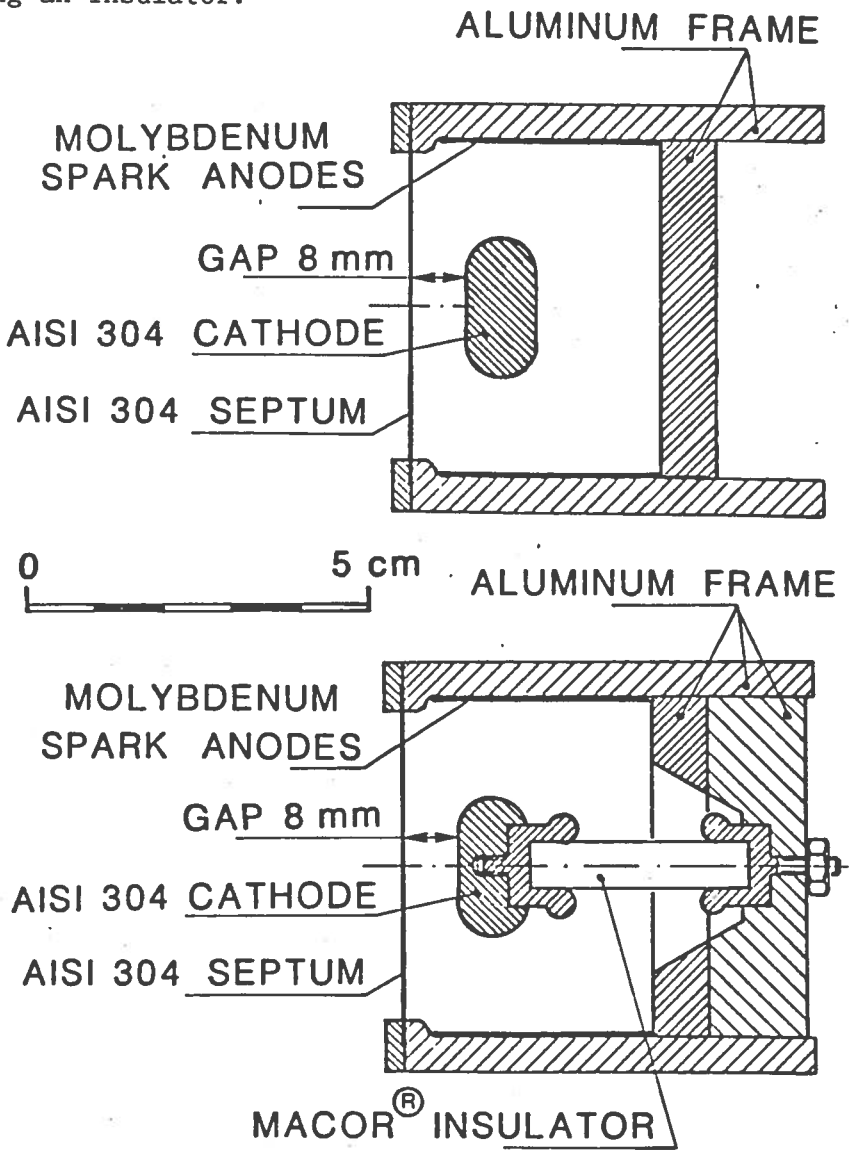

Figure 4.1: two sections of the prototype electrostatic deflector: a generic one and one along an insulator.

The main parameters of this geometry are:

1) electrode height: 20 mm
2) electrode radius of curvature: 5 mm (constant)
3) electrode straight section height: 10 mm
4) electrode-septum gap: 8 mm
5) vertical sparking gap: 15 mm
6) internal radial width of the grounded box: 50 mm
7) internal vertical height of the grounded box: 50 mm
8) insulator free surface length: 28 mm
9) insulator diameter: 9 mm

The electrical quantities relative to the first section were calculated, in particular the electric field along the electrode surface and in the gap: the complete data about the surface electric field are given in fig. 4.3 and 5.2. The mesh, the equipotential lines and the most important figures are shown in fig. 4.2.1-4.2.2 and table 5.1 (geometry G0) respectively. The field uniformity U(z) in the gap is computed as a function of the height from the median plane z:

$$U(z) = |E_{r\ elect}(z)-E_{r\ sept}(z)|/(2E_{nom}) \qquad (4.1)$$

The surface field enhancement F_e is given by:

$$F_e = E_{surf}/E_{nom} \qquad (4.2)$$

where $E_{r\ elect}$ and $E_{r\ sept}$ are the horizontal components of the gap electric field at the electrode and at the septum respectively, E_{surf} is the field modulus at the electrode surface and E_{nom} is the nominal gap electric field which is given by:

$$E_{nom} = V/d \qquad (4.3)$$

It should be noted that the field uniformity is rather poor compared with the required one, 1-2%[12], and that the field enhancement along the surface is quite high, resulting in a peak field at the design voltage, V=112 kV, of 197 kV/cm: moreover the electric field is very high even near the top of the electrode (161 kV/cm at 90^o in the same conditions), which is a very critical location in the magnetic field for electron emission sites, as we discussed in chapter 2. (see also ref. 10).

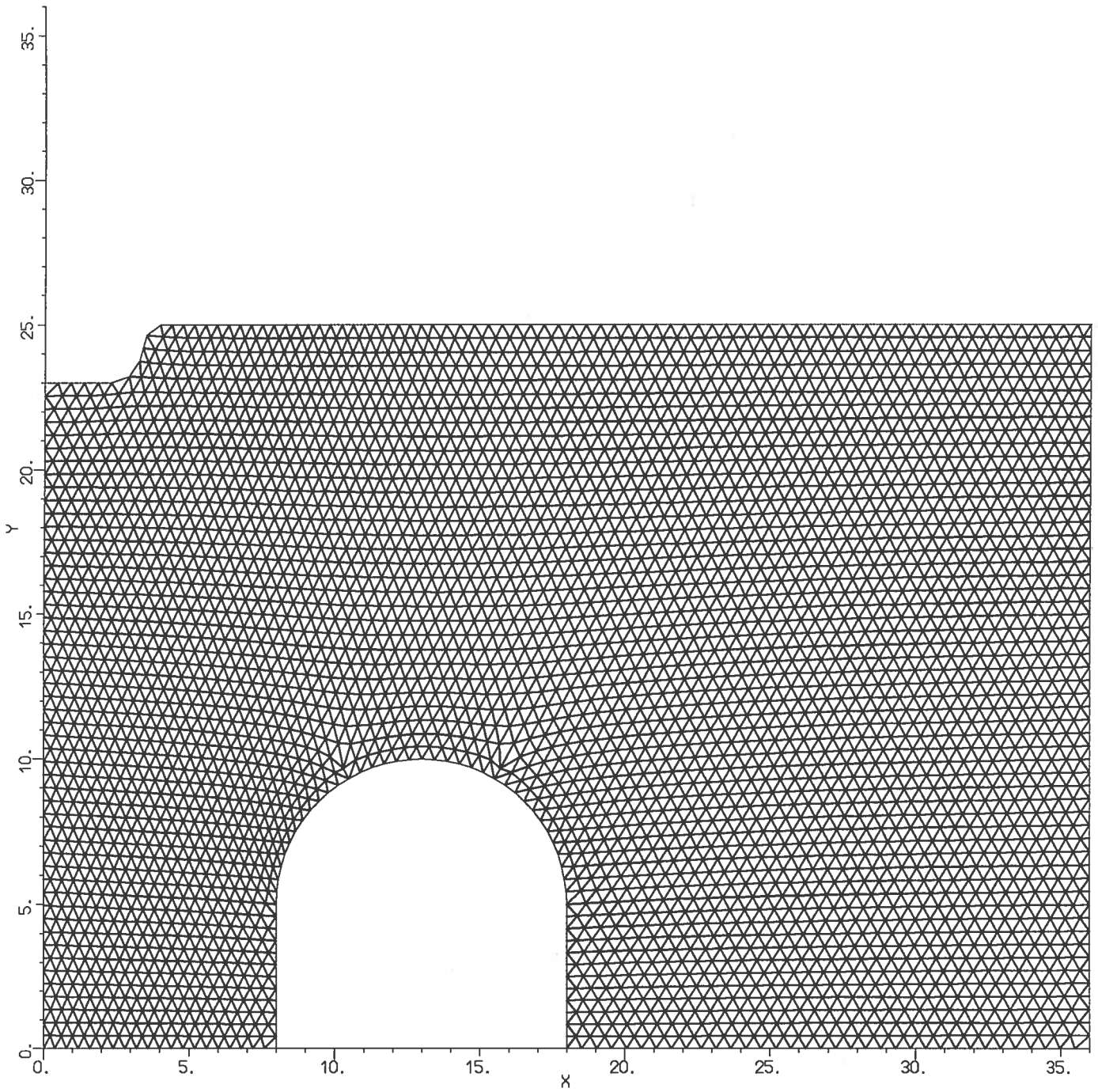

Figure 4.2.1: physical mesh used for the early prototype geometry (G0).

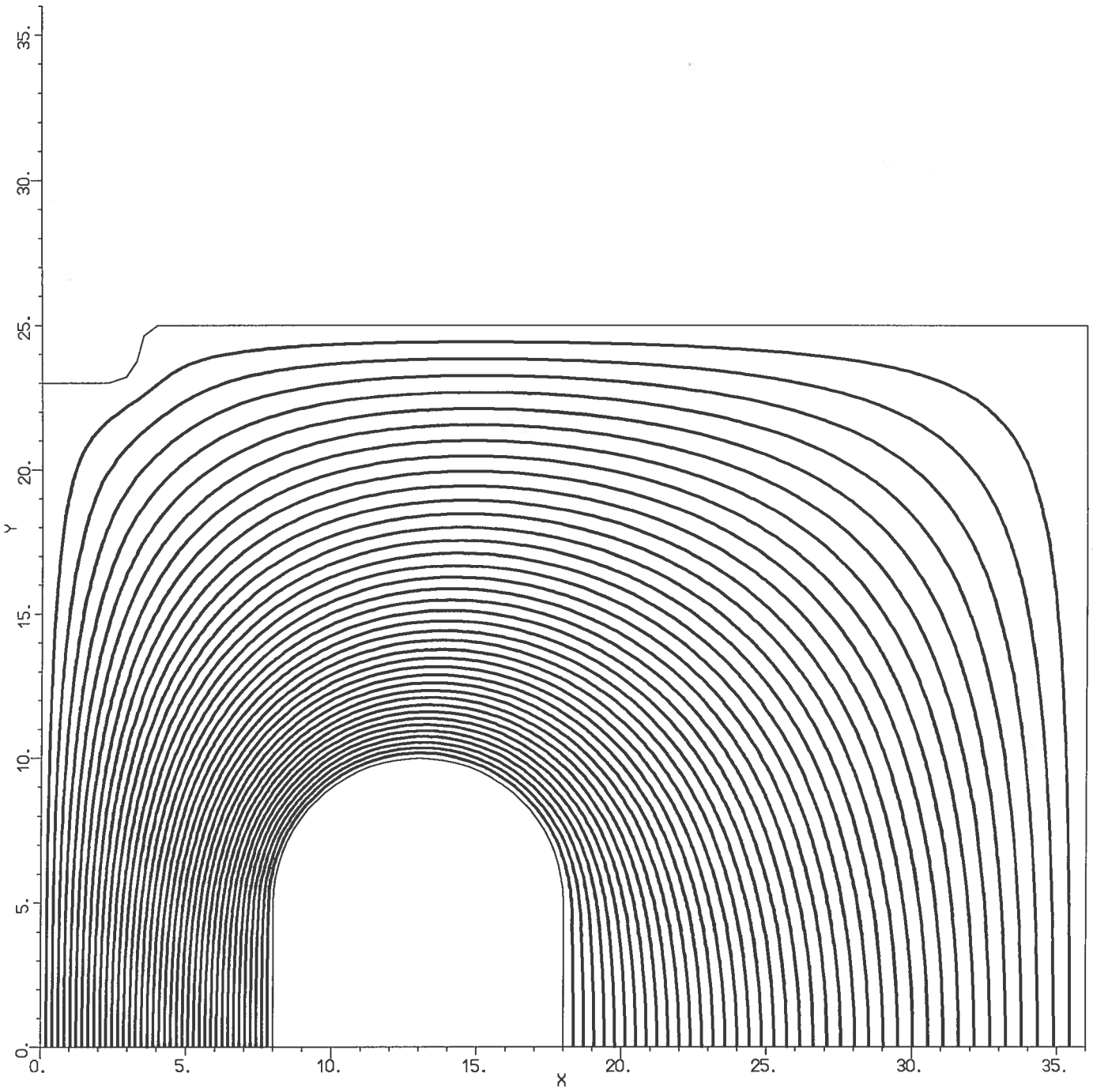

Figure 4.2.2: equipotential lines for the early prototype geometry (G0), plotted every 2.5% of the applied voltage.

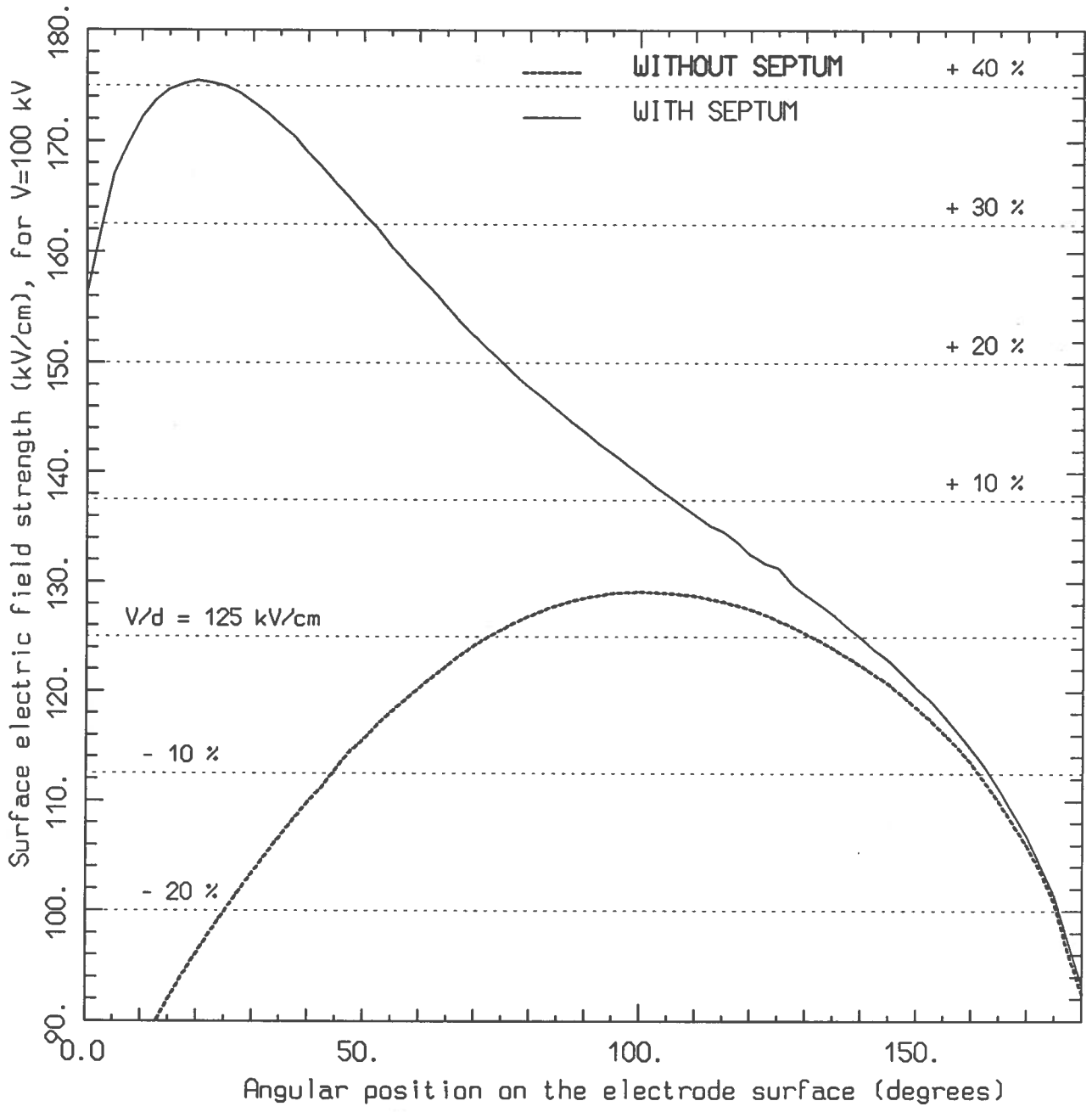

Figure 4.3: surface electric field along the electrode curvature for the geometry G0, with and without septum (angles counted clockwise), with a 100 kV applied voltage.

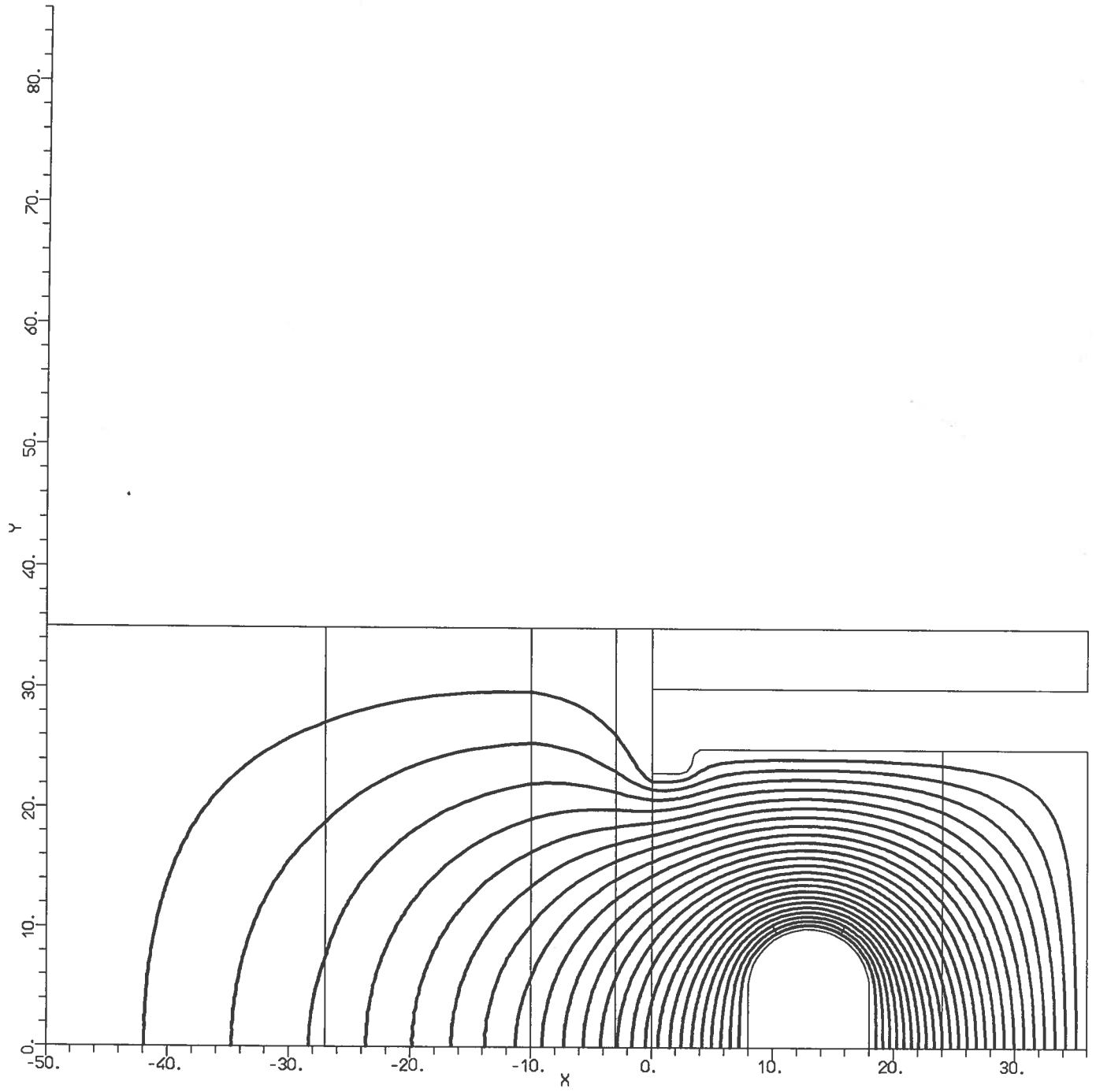

Figure 4.4: equipotential lines for geometry G0 without septum, plotted every 4% of the applied voltage.

Calculations were also carried out with the same geometry but with the septum removed for two reasons: first we wanted to realize how much was the relative influence of the septum and of the liner on the top electrode field, second we tried to explain the bad performances of the deflector prototype even when tested without septum. The results of the calculations are showed in fig. 4.3 and the equipotential lines in fig. 4.4: the maximum field occurred at about 90^{o} and its value was 144 kV/cm at V=112 kV. These figures show that most of the field enhancement at the top of the electrode is due to the liner influence rather than to the septum. This also underlines the problems caused by the reduced vertical clearance of the deflector.

5. - CALCULATION OF IMPROVED GEOMETRIES

In the previous chapters the reasons which show the need for an optimization of the deflector geometry were discussed. Moreover in the last chapter we have seen how the early geometry is critical for its high surface field and bad gap uniformity. Some of the parameters listed at the beginning of chapter 4 can not be changed without contrasting with the cyclotron requirements. These are:

-the grounded box overall height, which is fixed at 60 mm by the cyclotron pole clearance: with a reasonable thickness of 5 mm on the top and on the bottom for the walls, the liners and their screws, 50 mm is the maximum achievable internal vertical clearance of the deflector;

-the grounded box overall width, which is fixed at 55 mm by the clearance between the internal wall of the vacuum chamber and the last orbit of the ions to be extracted more externally: again with a reasonable figure of 5 mm for the wall thickness and the insulator support fixing, 50 mm is the maximum achievable internal radial clearance of the deflector;

-the gap between the electrode and the septum, whose minimum value is fixed at 8 mm by the expected beam size (a larger gap would require a higher voltage value);

-the electrode straight section height, which is fixed at 10 mm as a compromise between the opposite needs of the gap field uniformity, which requires a high straight section, and of the surface field on the curvature, which requires large radius and vertical sparking gap, therefore a small straight section;

-the insulator diameter, which can not be less than 7-9 mm in every point for mechanical (a fragile machinable glass-ceramic is used) and for experimental reasons (the present insulators work rather well).

As a consequence of these constraints on the deflector geometry the only parts one may try to optimize are the electrode radii. First some geometries with constant radius were tried in order to realize the effect of the different radii on the field uniformity in the gap and on field strength on the surface. These geometry are listed in table 5.1 with the most important data, computed for V=100 kV, E_{nom}=125 kV/cm. Some examples of the tested geometry are shown in fig. 5.1.1-5.1.3 with the equipotential lines plotted; the figure also shows the new grounded box section adopted.

TABLE 5.1 - GEOMETRIES WITH CONSTANT RADIUS

GEOM. NUMBER	CURVAT. RADIUS (mm)	UNIF. z=0 mm	UNIF. z=3 mm	PEAK FIELD (kV/cm) (E_{nom}=125kV/cm)	E_{surf} (kV/cm) at 60°	E_{surf} (kV/cm) at 90°	E_{surf} (kV/cm) at 120°	GRID# PITCH (deg)
G0*	5	3.4 %	6.3 %	175.5 at 20°	157.5	143.5	132.5	5
G1	5	3.4 %	6.3 %	175.5 at 20°	157.	141.5	128.	5
G2	7	2.7 %	4.9 %	161.5 at 16°	139.5	130.	119.	4
G3	7.5	2.5 %	4.6 %	159.5 at 14.4°	137.	129.	118.5	3.6
G4	8	2.4 %	4.4 %	157.5 at 12.6°	135.	129.	119.	3.6
G5	9	2.2 %	4.1 %	154. at 12°	132.5	131.	121.	3

#The field strength is computed at the half integer multiples of the grid pitch
*This geometry is the old one, it differs from G1 only for the different grounded box section

The data presented in table 5.1 show that the optimum radius to minimize E_{surf} at 90° is about 7.5 mm, a value which is in very good agreement with the value given by the very simple analytical model of a conducting cylinder with an grounded plane with fixed distance between the cylinder axis and the plane; it shows also that, obviously, the larger the radius the better is the field uniformity in the gap and the lower is the peak field. It is also clear that a further increase in the radius would give only small advantages in the peak field and in the uniformity but would be unfavorable for the field strength near the top and for the insulator length, which decreases of 2 mm

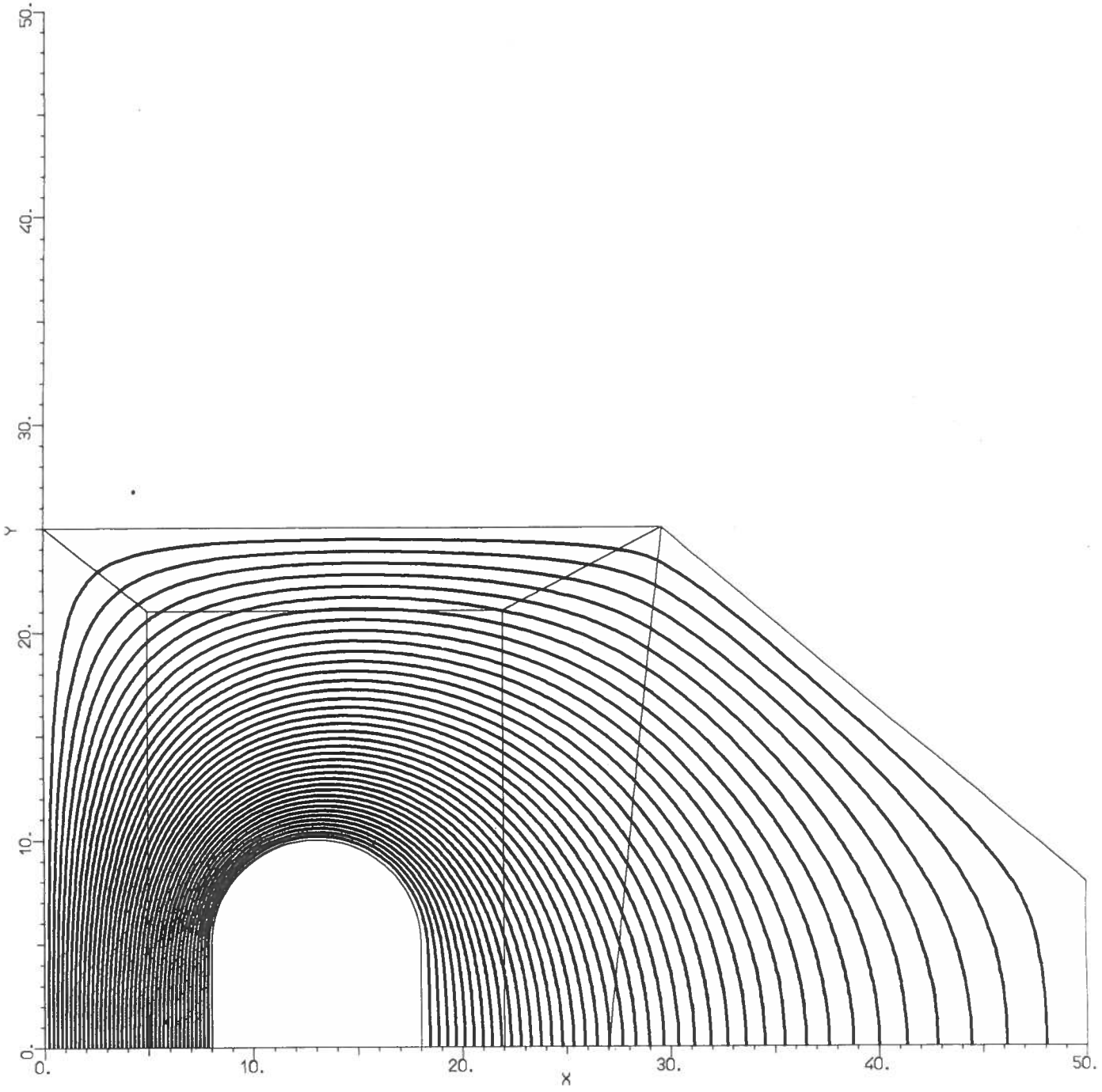

Figure 5.1.1: equipotential lines, plotted every 2.5% of the applied voltage, for the deflector geometry G1 (HV electrode with a costant radius of 5 mm).

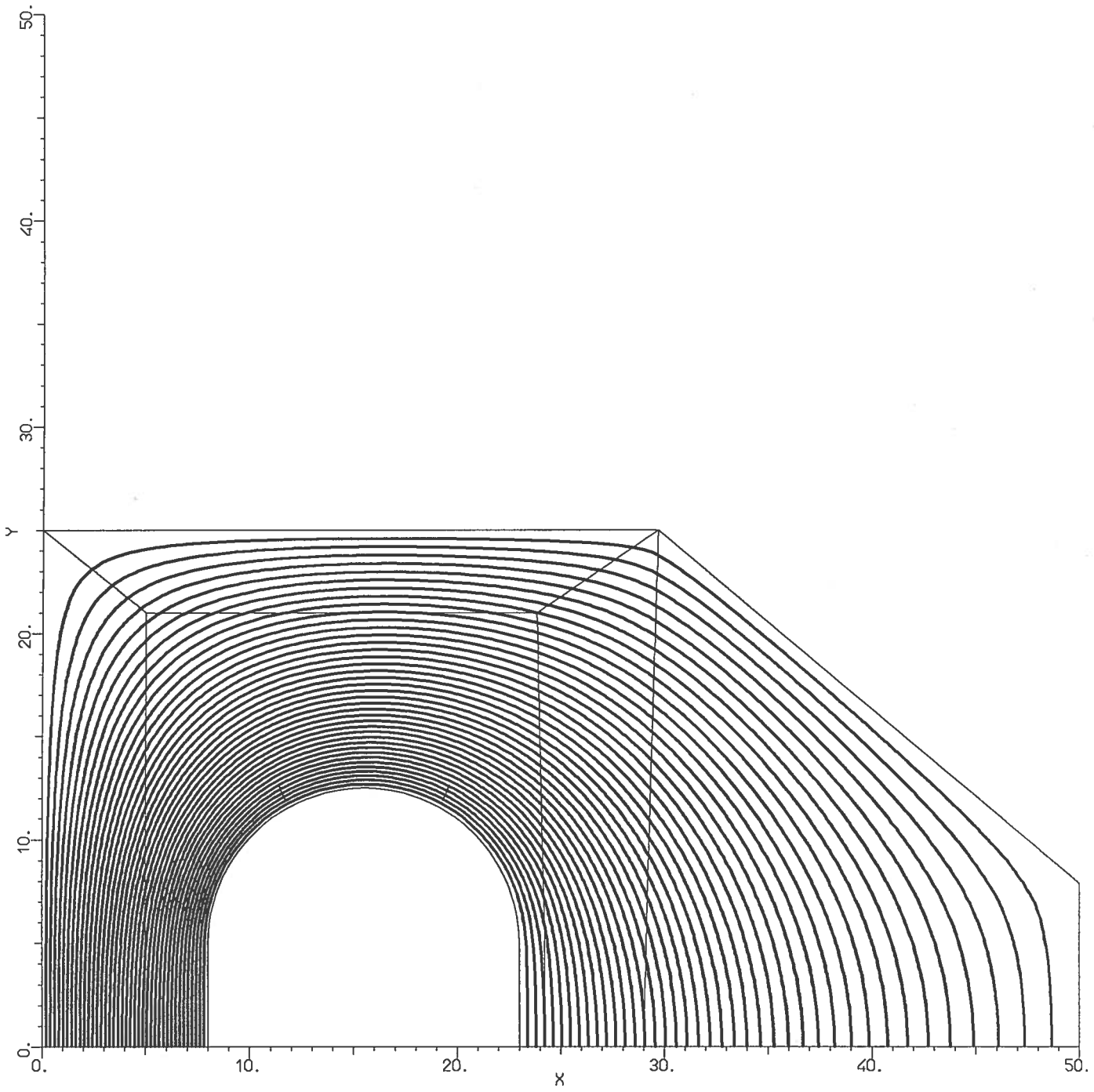

Figure 5.1.2: equipotential lines, plotted every 2.5% of the applied voltage, for the deflector geometry G3 (HV electrode with a costant radius of 7.5 mm).

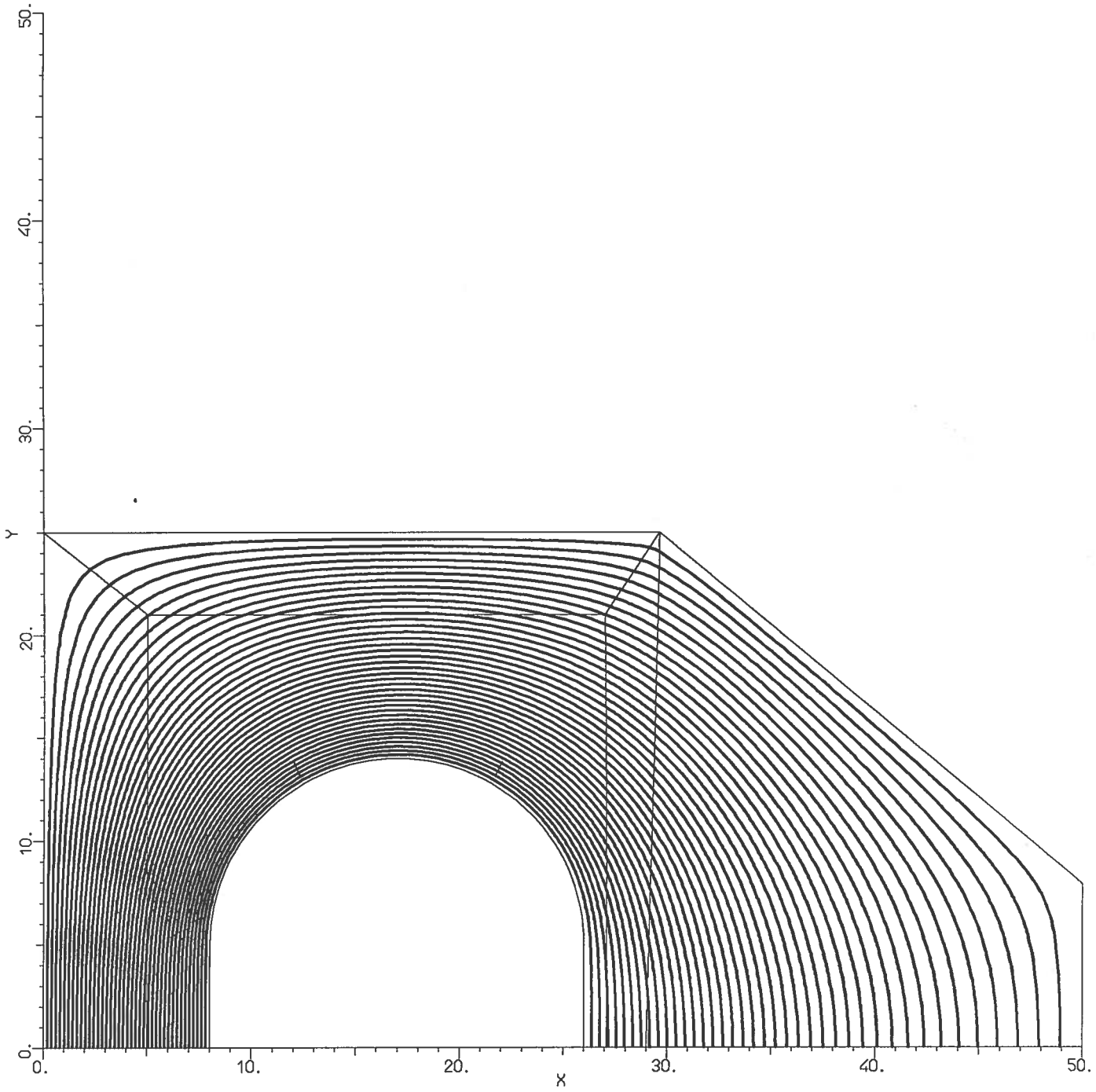

Figure 5.1.3: equipotential lines, plotted every 2.5% of the applied voltage, for the deflector geometry G5 (HV electrode with a costant radius of 9 mm).

for every 1 mm increase in the electrode radius. As the insulator original length gave only small safety margin at the design voltage during the experimental tests, it was decided to check geometries with various radii, in order to get the same results of the best geometries of table 5.1 with a limited decrease in the insulator length; of course the study of a new fixing for the insulator is implied. The three geometries with non-constant radii which have given the best results are listed in table 5.2 with the same data of table 5.1: for comparison the geometry G0 is also reported.

TABLE 5.2 - GEOMETRIES WITH VARIOUS RADII

GEOM. NUMBER	CURVAT. RADII[@] (mm)	UNIF. z=0 mm	UNIF. z=3 mm	PEAK FIELD (kV/cm) (E_{nom}=125kV/cm)	E_{surf} (kV/cm) at 60°	E_{surf} (kV/cm) at 90°	E_{surf} (kV/cm) at 120°	GRID[#] PITCH (deg)
G0*	5	3.4 %	6.3 %	175.5 at 20°	157.5	143.5	132.5	5
G6	10-119° 5- 61°	2.0 %	3.7 %	151. at 11.2°	132.	136.5	138.5	2.8 5
G7	12- 35° 7-125°	1.8 %	3.3 %	148.5 at 82°	147.5	148.	136.	2.3 4
G8	8-135° 4- 45°	2.4 %	4.4 %	157.5 at 12.6°	135.	129.5	121.5	3.6 5

[@]The angular extension of the constant radius section is indicated near the radius used

[#]The field strength is computed at the half integer multiples of the grid pitch, the different values of the pitch are referred to the different radii

*This geometry is the old one, it differs from G1 only for the different grounded box section

In fig. 5.2.1-5.2.4 some examples of meshes and equipotential lines plots are shown for these two radii geometries.

In fig. 5.3 the surface field strength is reported as a function of the curvature angle for the five geometries, G0, G3, G6, G7 and G8. It is possible to note that the G7 field is nearly constant at its maximum value from 0° to over 100°: this geometry is nearly the optimum for minimizing the peak field, as, obviously, every attempt to decrease the field somewhere in the first 100°, would cause a field increase elsewhere. However the electric field strength at the top of the electrode for G7 is high, even more than in G0, so this geometry is believed to be not suitable for operating in the magnetic field; the 18% reduction of the peak field from the original one is anyhow notable. The geometry which is believed to be the most suitable is G8: in fact with a moderate increase in the maximum field (9 kV/cm, 6%) in

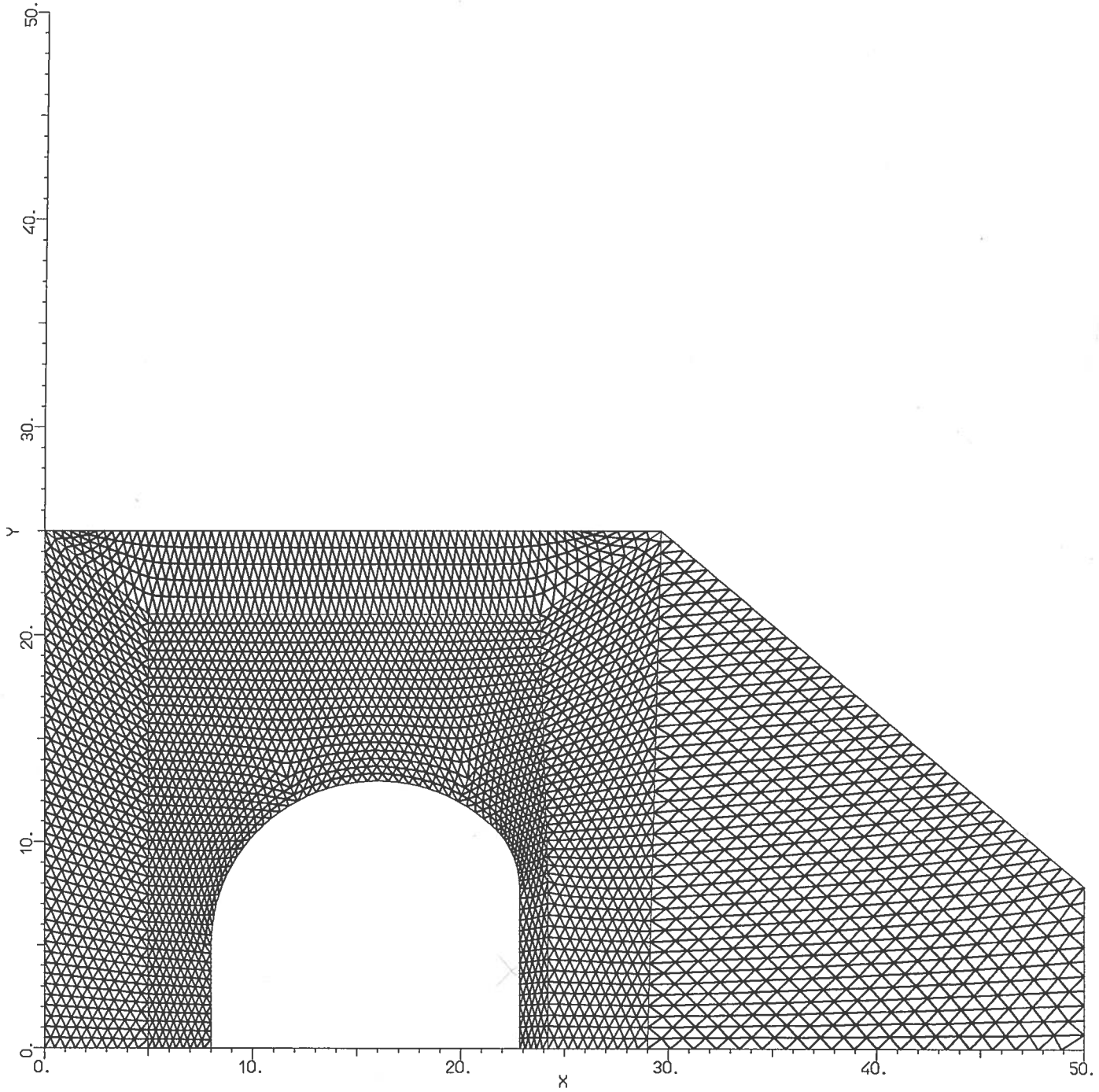

Figure 5.2.1: physical mesh for the deflector geometry G8 (HV electrode with 8 and 4 mm radii).

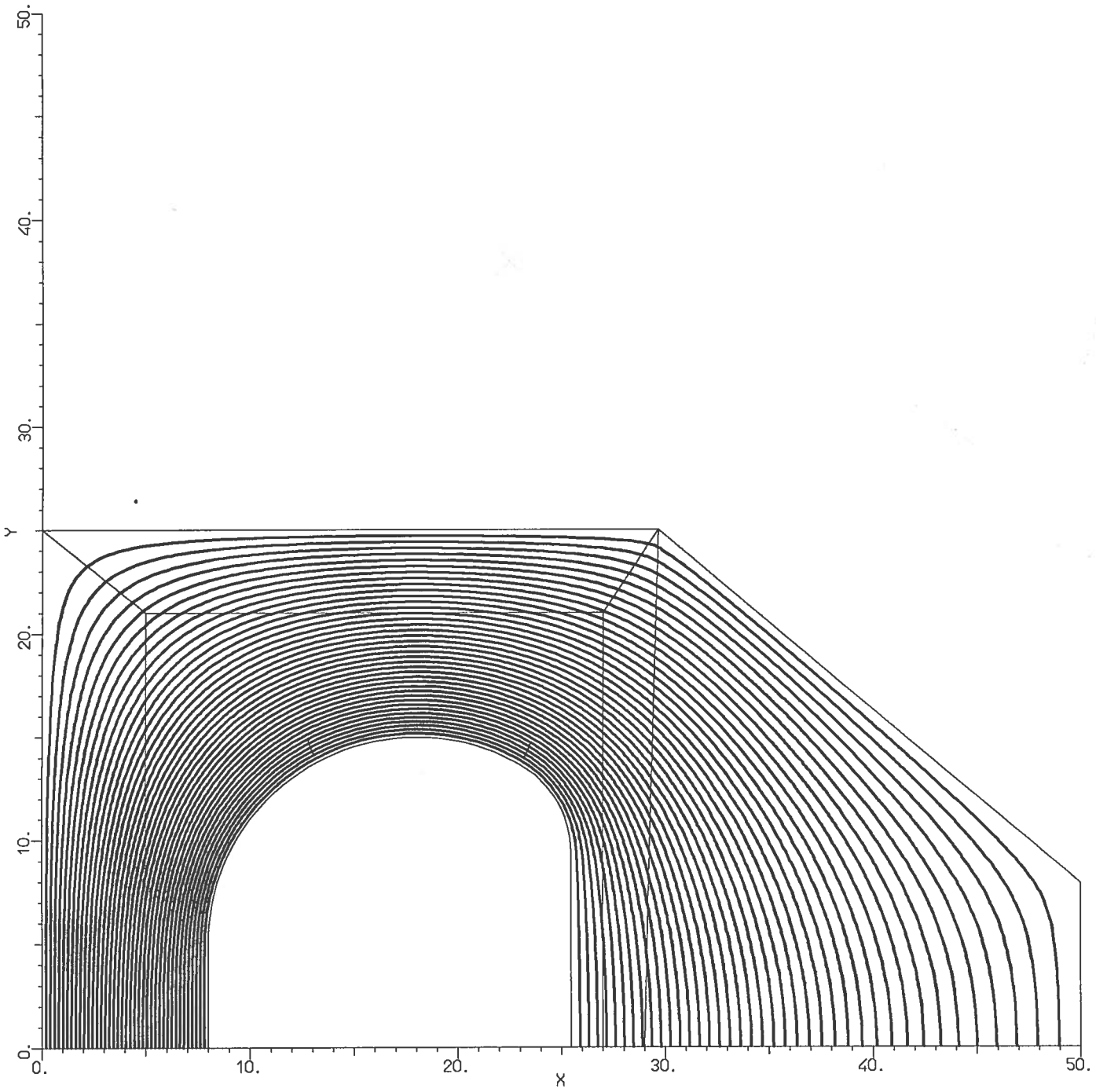

Figure 5.2.2: equipotential lines, plotted every 2.5% of the applied voltage, for the deflector geometry G6 (HV electrode with 10 and 5 mm radii).

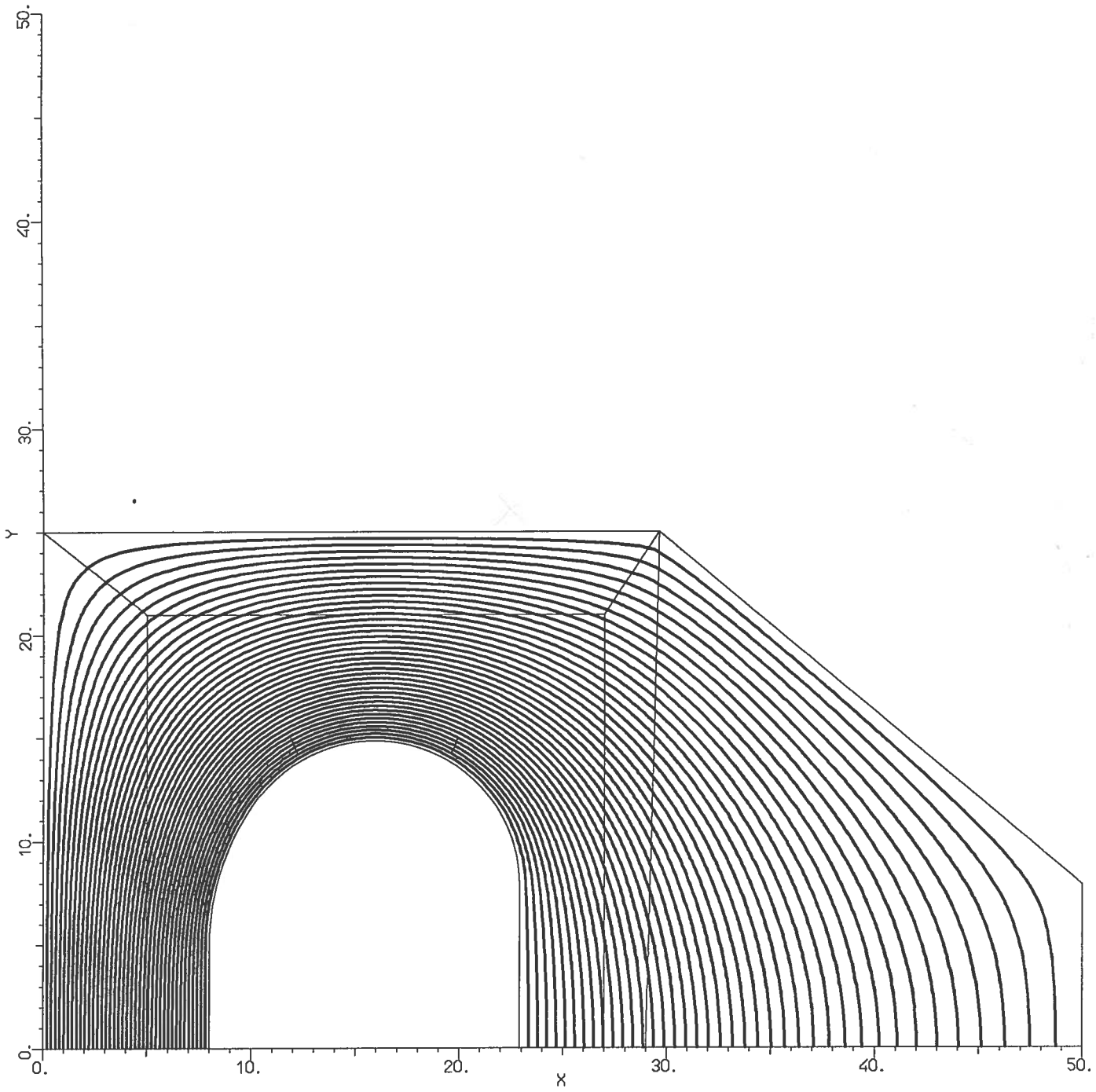

Figure 5.2.3: equipotential lines, plotted every 2.5% of the applied voltage, for the deflector geometry G7 (HV electrode with 12 and 7 mm radii).

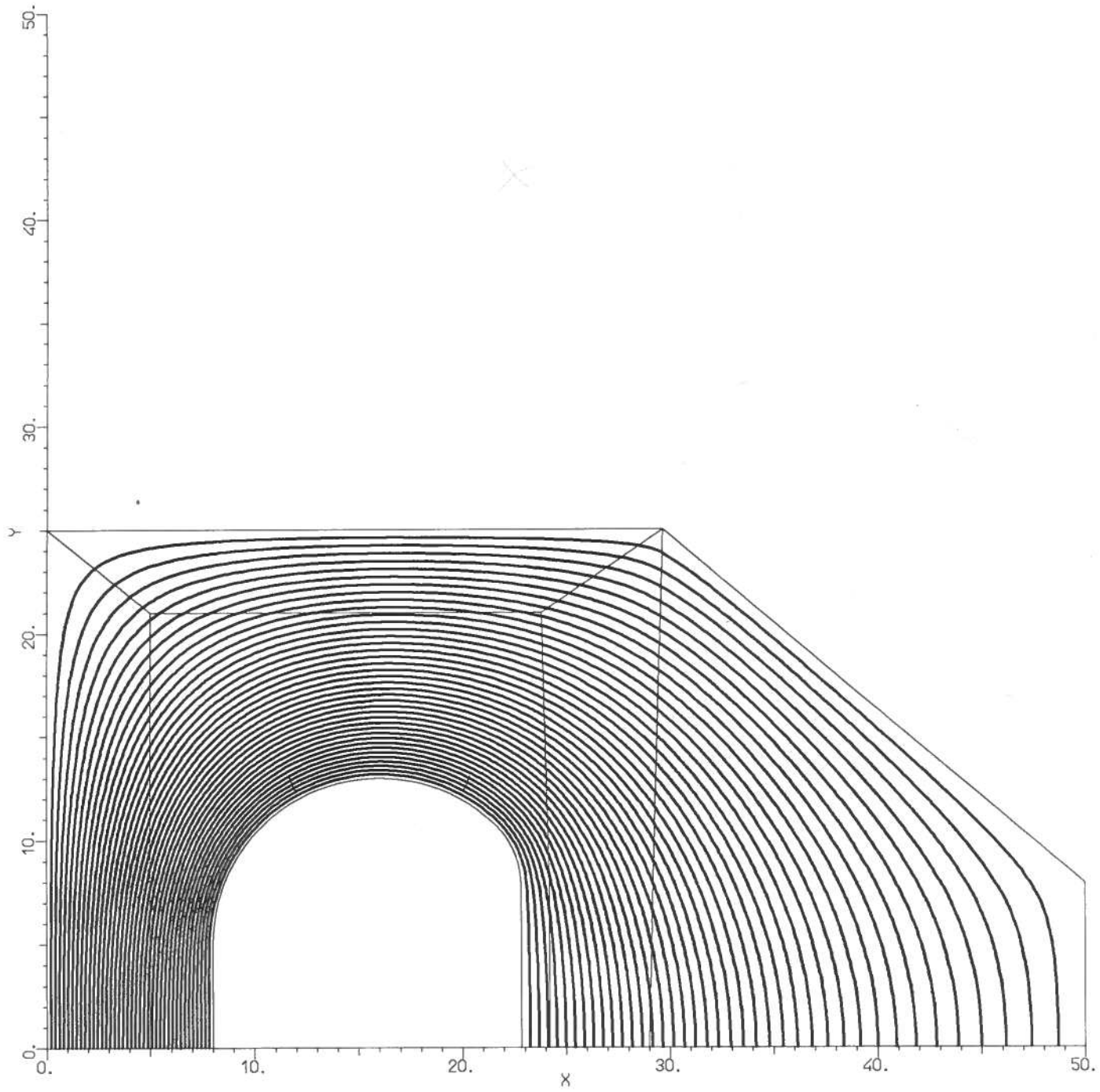

Figure 5.2.4: equipotential lines, plotted every 2.5% of the applied voltage, for the deflector geometry G8 (HV electrode with 8 and 4 mmm radii).

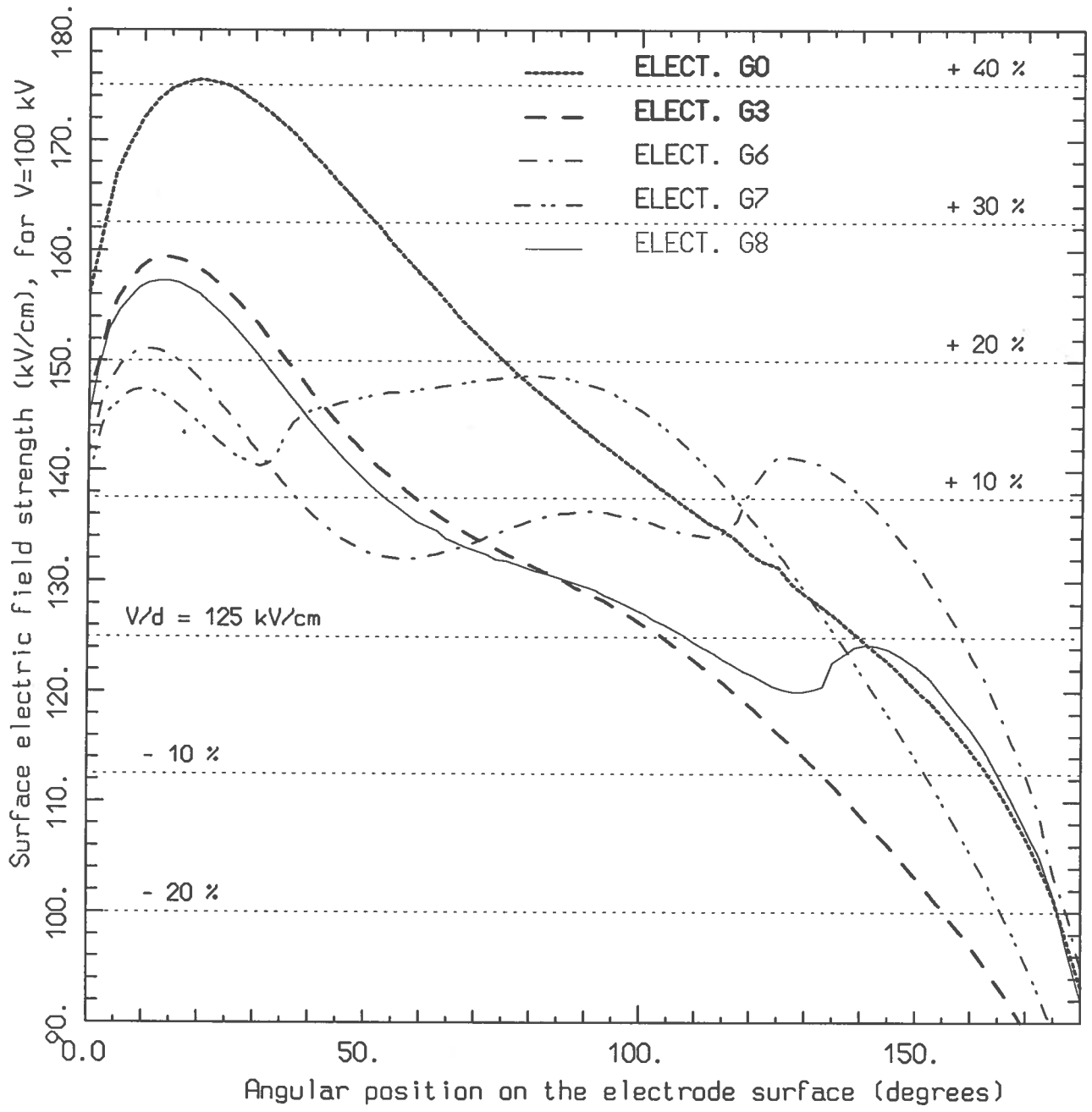

Figure 5.3: surface electric field strength on the electrode curvature for some of the tested geometry, with a 100 kV applied voltage.

comparison with the best obtainable, the 60°, 90° and 120° field strength are respectively 17%, 11% and 11% less than in G0. Of course this geometry has, from the surface field strength point of view, no advantage with respect to G3-G5 and indeed is more complicate to machine: however it may be preferable because the larger back straight section in the electrode, 15.7 versus 10 mm, with roughly the same thickness, 14.8 mm, allows longer insulators with a better shielded fixing. In fact a constant radius geometry with radius 7-8 mm, if used with an insulator fixing like the one used until now (see fig. 4.1), implies a length reduction of 4-6 mm, while with geometries like G6-G8 a fixing completely included in the electrode thickness without a significant length reduction can be designed, with the further advantage that a similar fixing is likely to be less critical for the surface field in the axial direction than the old one (for further details on the insulator fixing problem see the next chapter). A small further reduction (few kV/cm at most) in the electric field strength near the top of the electrode could perhaps be achieved only if a small radius, less than 6 mm, were used for the first part of the curvature, followed by a larger one, 8-9 mm, for the top angles: however this would imply a high peak field, near 170 kV/cm at V=100 kV, a bad gap field uniformity and the need of a third radius, shorter than the first and the second, to complete the curvature with enough space for the insulator fixing in the back: therefore it was decided to be restricted to two-radii geometries.

With regard to the gap field uniformity the values listed in table 5.1 and 5.2 would seem too poor: however beam dynamics calculations[12] showed no significant deterioration of the beam properties due to such a poor uniformity. Moreover it must be noticed that the uniformity of the curved deflector will be approximately a factor $\Delta R/R$ (ΔR being the gap width and R the deflector curvature) better than the straight deflector one. Therefore with a typical curvature radius of 750 mm and the gap 8 mm wide the figures listed must be decreased of about 1%, so resulting in more acceptable values (typically <2%).

6. - DESIGN OF THE INSULATOR SUPPORTS FOR THE NEW GEOMETRIES

A detailed view of the old insulator geometry is shown in fig. 6.1; the insulator is a threaded Macor cylinder which is mounted by heating the stainless steel supports until 300-350 C° to allow the insertion of the insulator, which is a few hundredths of millimeter larger than the support hole. A fairly good breakdown voltage was achieved with this insulator geometry, however it is not completely satisfactory for the fragility of the

mounting and for the electric field strength on the corona ring around the insulator fixing which seems to be very high as several pits above it were found on the liner surface during the tests in the magnetic field. Moreover, as it was discussed in the last chapter, this kind of support implies an insulator length reduction when used with electrode thicker than the original one.

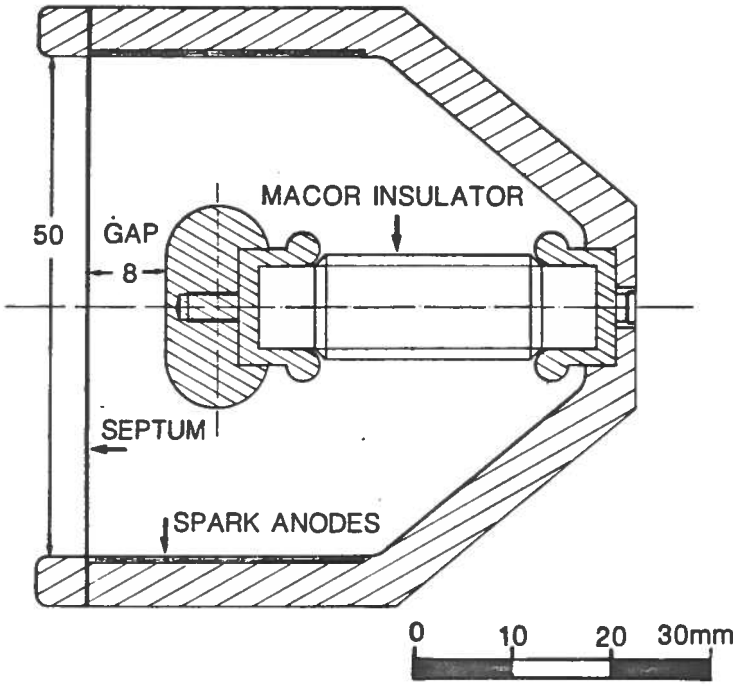

Figure 6.1: detailed sketch of the early insulator geometry in the new deflector grounded box (geom. I0).

Two new insulator geometries, which were suitable for the new electrode geometries, were studied; the former was designed so as to be nearly the same for the G6, G7 and G8 geometries, the latter was a very simple one designed for the G3 geometry. All the details of the first new insulator geometry are shown in fig. 6.2, for the G8 electrode and the insulator brazed to the supports. The insulator and the supports are the same for the three electrodes (G6, G7 and G8) both in the version with the insulator brazed and in that with the old fixing. The insulator free length between the two supports is 28.8 mm versus 23.1 mm of the old geometry, the diameter is 9 mm as the old one. The second new insulator geometry is shown in fig. 6.3 with the insulator brazed to the support; the insulator free length and diameter are 27 and 8 mm.

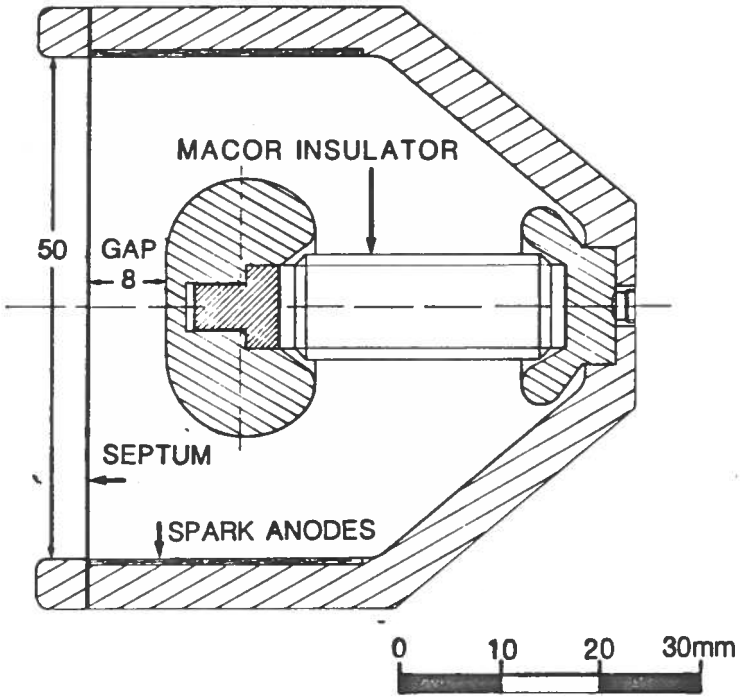

Figure 6.2: detailed sketch of the first new insulator geometry I1.

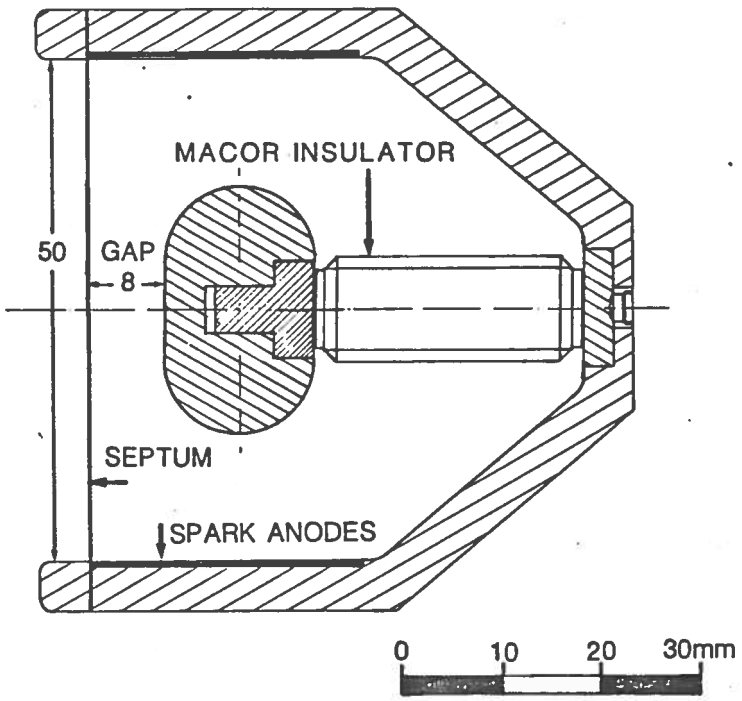

Figure 6.3: detailed sketch of the second new insulator geometry I2.

While for the first new fixing an effort was made to design a well shielded support in order to minimize the field strength near the triple junction (vacuum, metal and dielectric), the second one was designed so simply to achieve a good insulator length with the thickness and the short straight section of the G3 geometry. No particular effort was made to improve the electrostatic performances of the insulator itself because of the difficulty in simulating the charging processes of the insulator surface (see ref. 5, last chapter, and references therein) and in evaluating the electric field strength near the triple junction (vacuum, metal and dielectric) with the standard POISSON field editing package.

Calculations were mainly carried out to check that the electric field strength on the metal surface of the insulator fixings were less critical than on the corona ring of the old geometry: of course these calculations are only approximate because of the intrinsic three-dimensional geometry of the old and the new insulator fixings.

In particular, among the two radii geometries, only the G8 geometry was checked because it was believed to be the most suitable and moreover the surface field strength near the insulator hole have to be worse in this case than in G7, the other interesting geometry, for the shorter final radius (4 mm vs. 7 mm); two calculations were carried out, both with the insulator brazed (no particular difference is expected in the field near the transition between the radius 4 mm and the hole, which is the point we want to investigate, for the other way of fixing), differing only for the problem symmetry which was respectively cartesian and cylindrical. In the first the insulator is considered as an infinite slab with a thickness equal to the diameter; of course this is not true but this way of modeling seems to be reasonable for an estimate of the electric field strength on a vertical section of the electrode passing through an insulator, except for the points deep inside the hole. In the second the problem symmetry axis is coincident with the insulator axis and the electrode is considered as a disk with diameter equal to its height: this way of modeling seems to be adequate only for evaluating the field in the areas inside the insulator hole. Two analogous calculations were also performed for the old and the other new insulator fixing.

The computed field strength for all the three fixings is shown in fig. 6.4 as a function of the distance along the metal surface from the triple junction: the name I0 refers to the old geometry, I1 and I2 to respectively the G8 and G3 electrode insulators.

An insulator with ε_r=5.8, the relative dielectric constant of Macor, was used in all the calculations: no attempt was made to simulate the

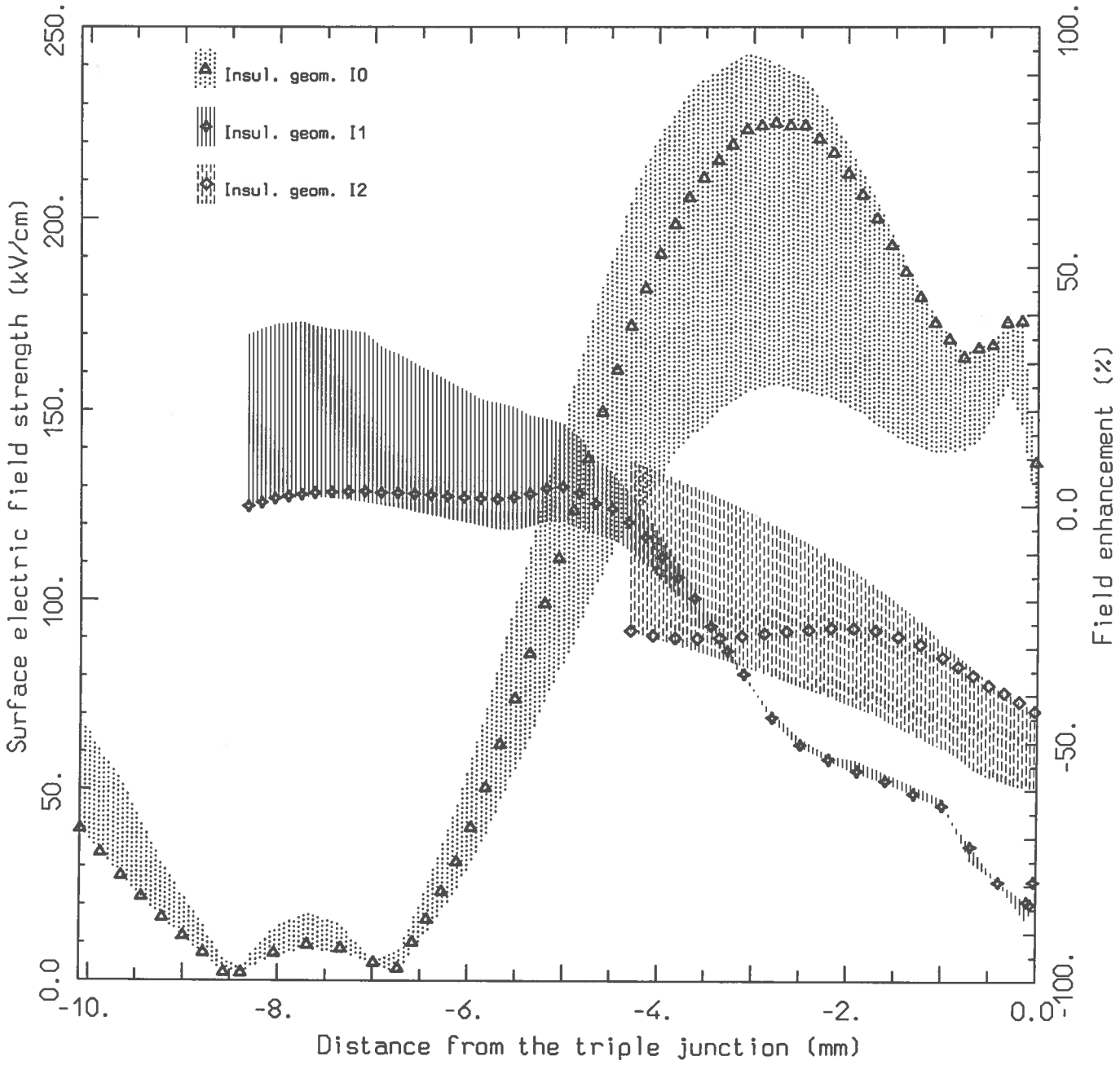

Figure 6.4: surface electric field strength along the insulator fixing for the three geometries considered in the calculations and a 100 kV applied voltage (see text for details).

insulator threading since its effect on the surface field on the electric surfaces is believed to be less than the accuracy of the calculations. The boundaries of the shadowed area are formed by the cylindrical and cartesian approximation results: the error in the last millimeter can be estimated at ±30%, for IO and I1, and ±10% for I2 mainly because of the difficulty in computing fields with the POISSON fit option near a transition between two different materials, while for all other points the precision is believed the same of the cartesian and cylindrical problems discussed in the previous chapters. The symbols represent a reasonable interpolation between the two boundaries which takes into account the distance between the point under consideration and the two points at which the problem can be considered fully cartesian or cylindrical: the triple junction is used as the last point for all the geometries, while the first is chosen looking at the computed field in the two symmetries and at the geometry. Clearly the choice of this point may be somewhat arbitrary, but the actual values of the field strength along a vertical section of the insulator fixings reasonably lie in the shadowed areas not too far from the printed symbols.

In fig. 6.5.1-4, 6.6.1-4, 6.7.1-4 the meshes and the equipotential lines for the insulator fixing zone are shown for, respectively, IO, I1 and I2 in cartesian and cylindrical symmetry.

The fields plotted in fig. 6.4 show how much critical was the old fixing geometry: the peak field value is likely to be well over 200 kV/cm with a 100 kV voltage applied. The new geometries are likely to reduce the troubles connected with discharges occurring between the electrode and the liners near the insulators. In particular I1 has a very low field near the metal-insulator junction and moreover provides a shielding of the initial area of the insulator which may result in a reduced metallization of the HV end of the insulator.

However it must be noticed that these are theoretical results: actually the need for removable insulators implies a mechanical discontinuity (see fig. 6.2-6.3) in the insulator fixing which may results in a significant enhancement of the field strength, so reducing the improvement with respect to IO, which has the discontinuity in a very low field area. This problem is likely to be more serious for I2, where the discontinuity is not shielded at all. Moreover the eventual use of insulators mounted in the old way surely will further increase the field strength near the triple junction with respect to the value showed in fig. 6.4.

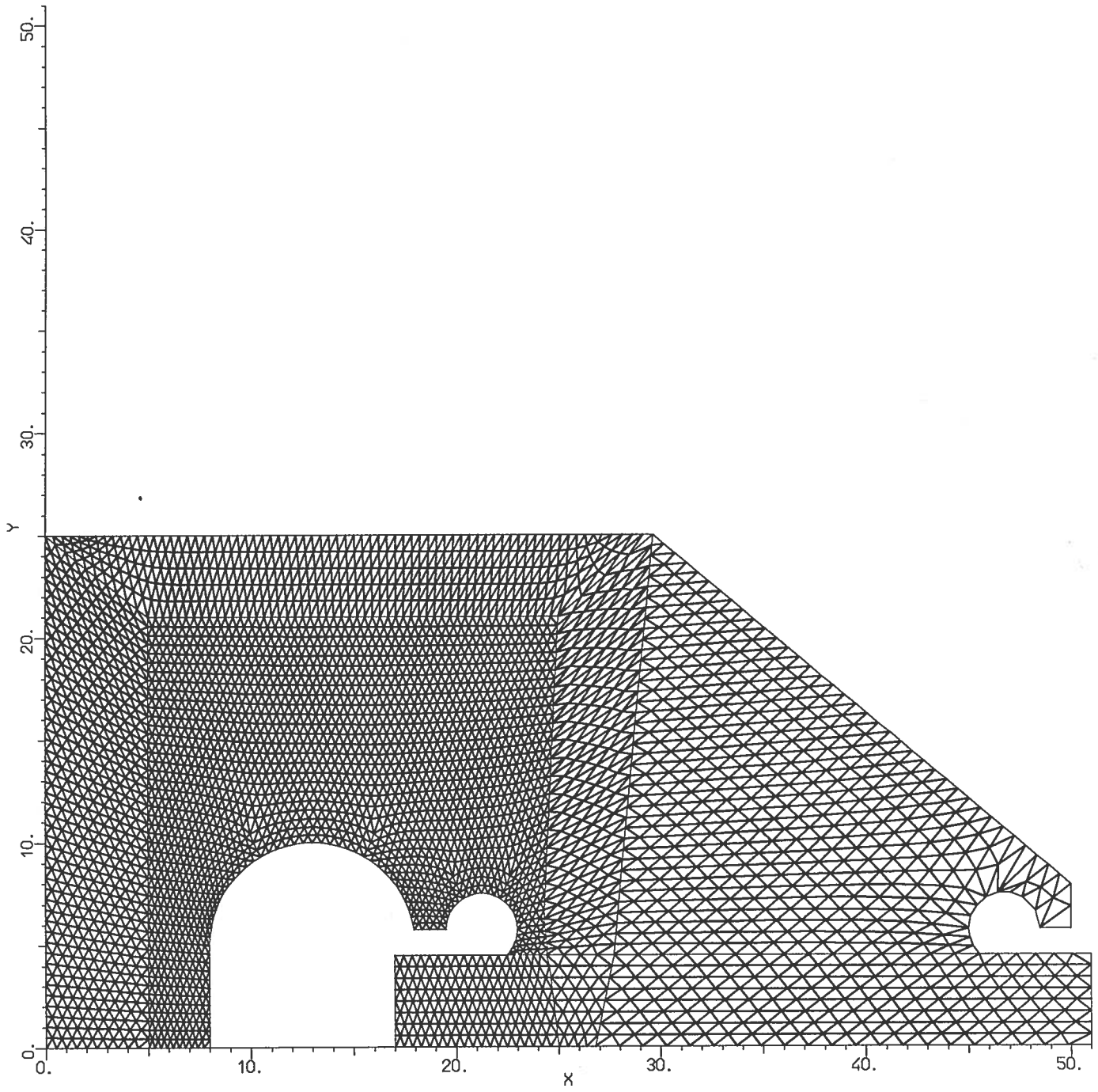

Figure 6.5.1: physical mesh for the insulator fixing zone (geometry I0), cartesian symmetry.

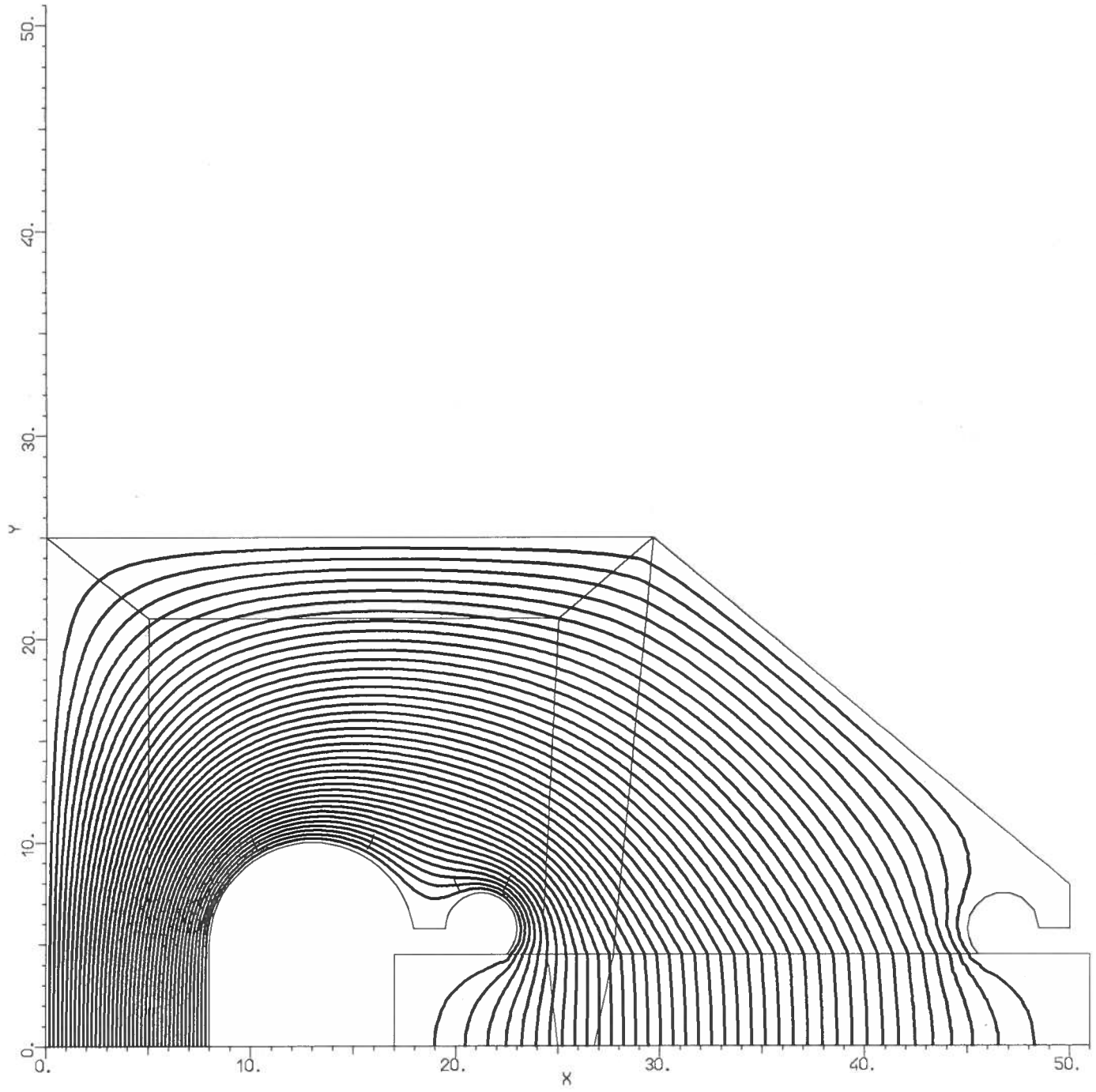

Figure 6.5.2: equipotential lines (step 2.5% of the applied voltage) for the insulator fixing zone (geometry I0), cartesian symmetry.

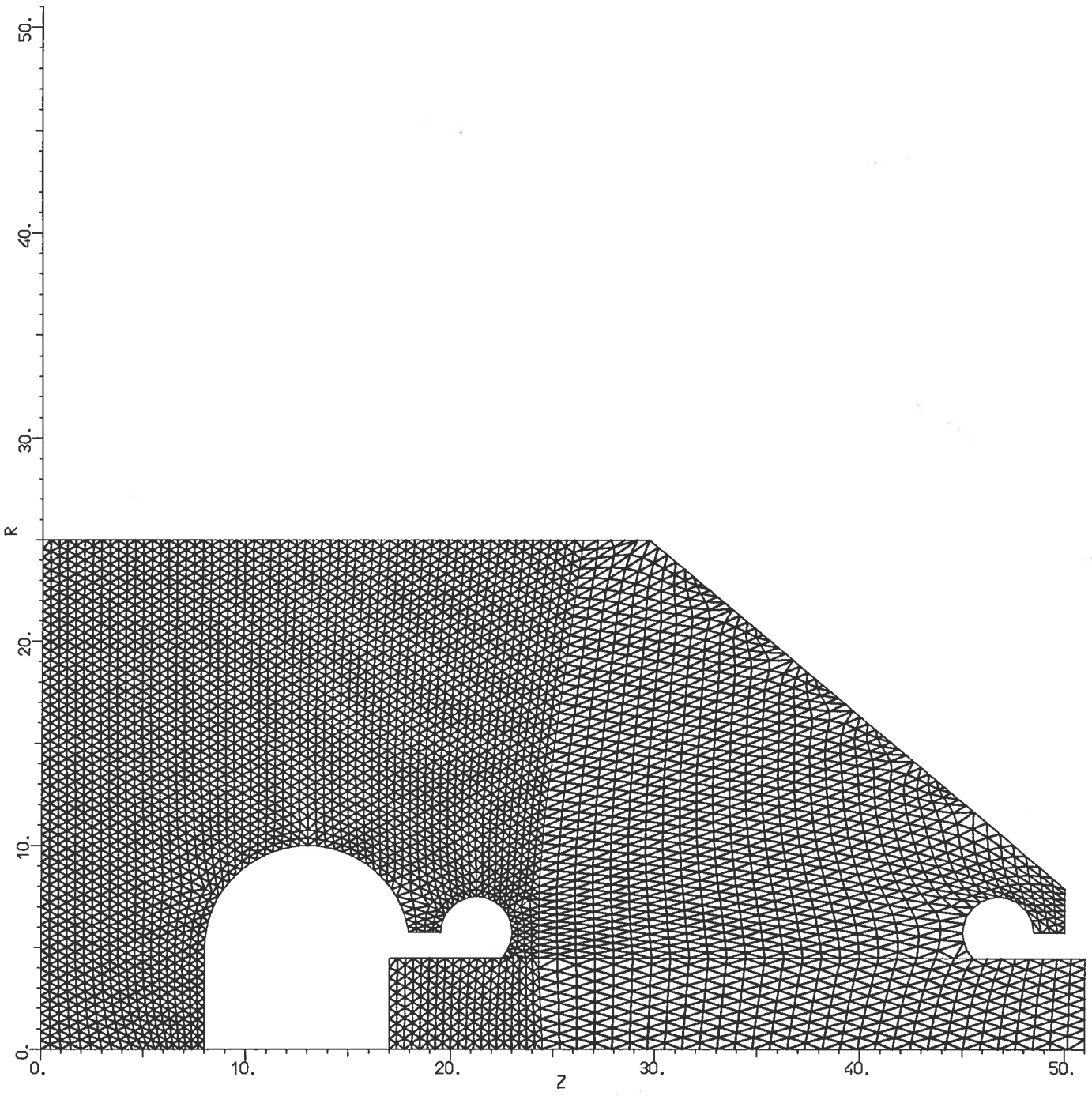

Figure 6.5.3: physical mesh for the insulator fixing zone (geometry I0), cylindrical symmetry.

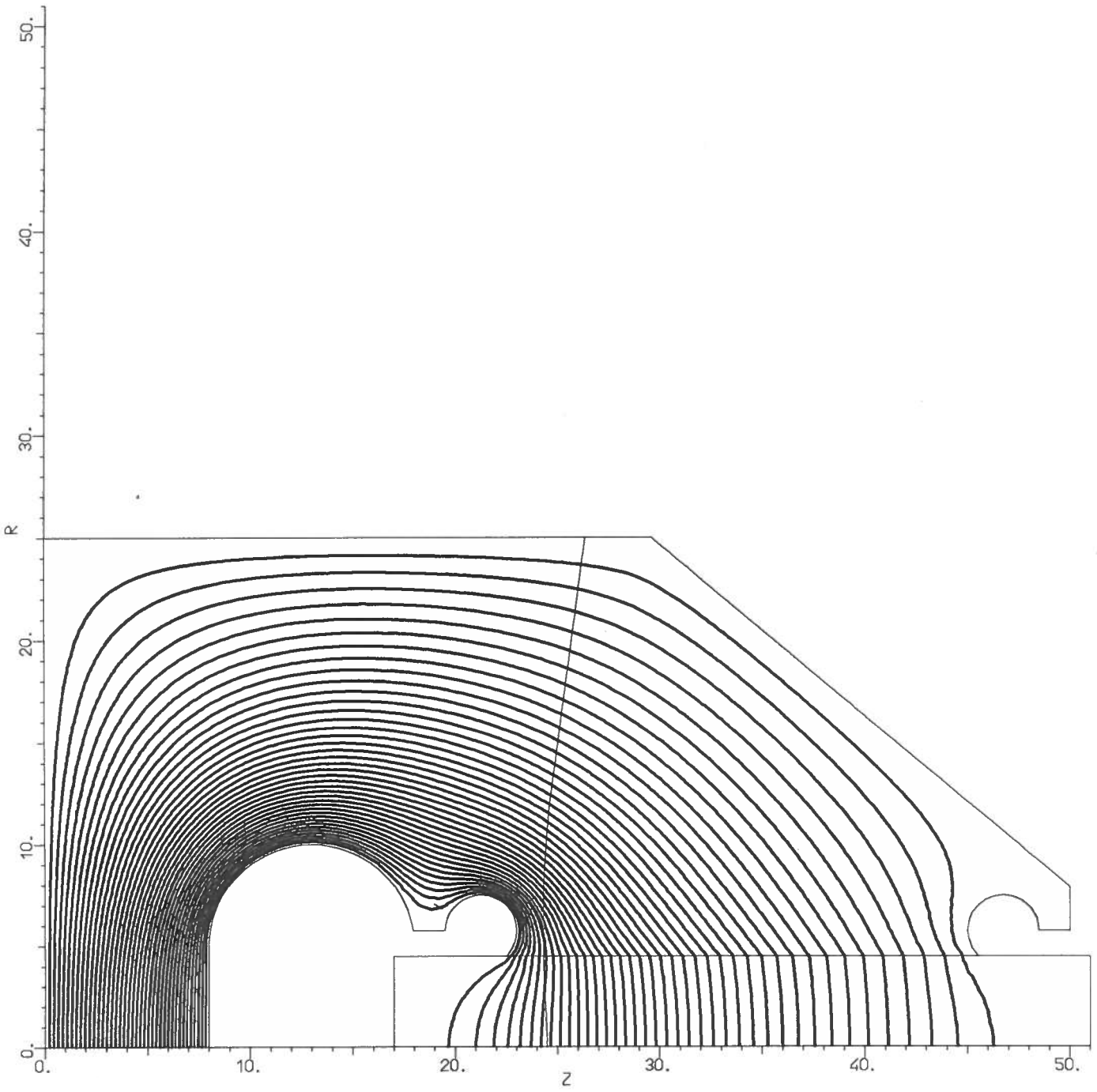

Figure 6.5.4: equipotential lines (step 2.5% of the applied voltage) for the insulator fixing zone (geometry I0), cylindrical symmetry.

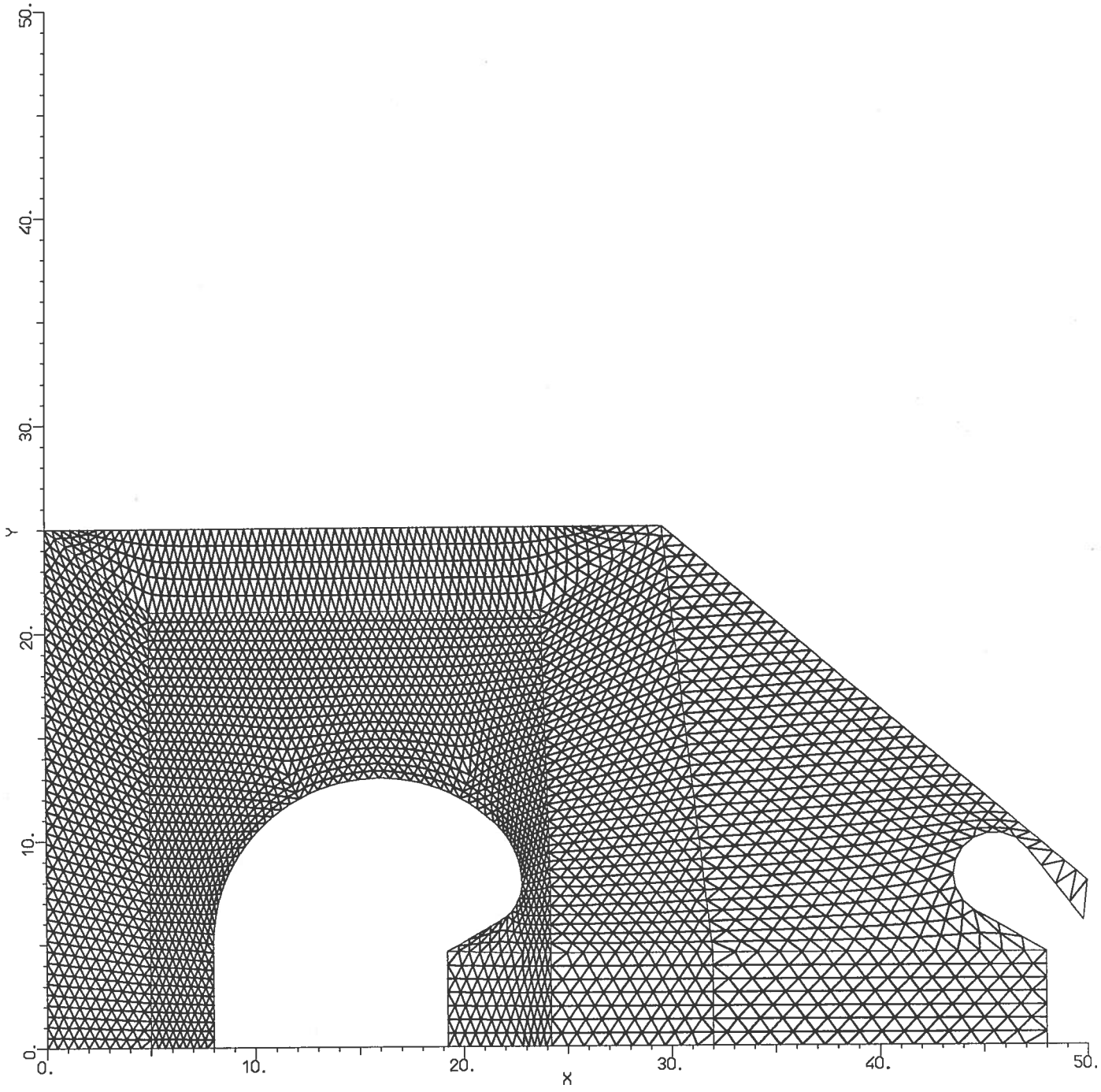

Figure 6.6.1: physical mesh for the insulator fixing zone (geometry I1), cartesian symmetry.

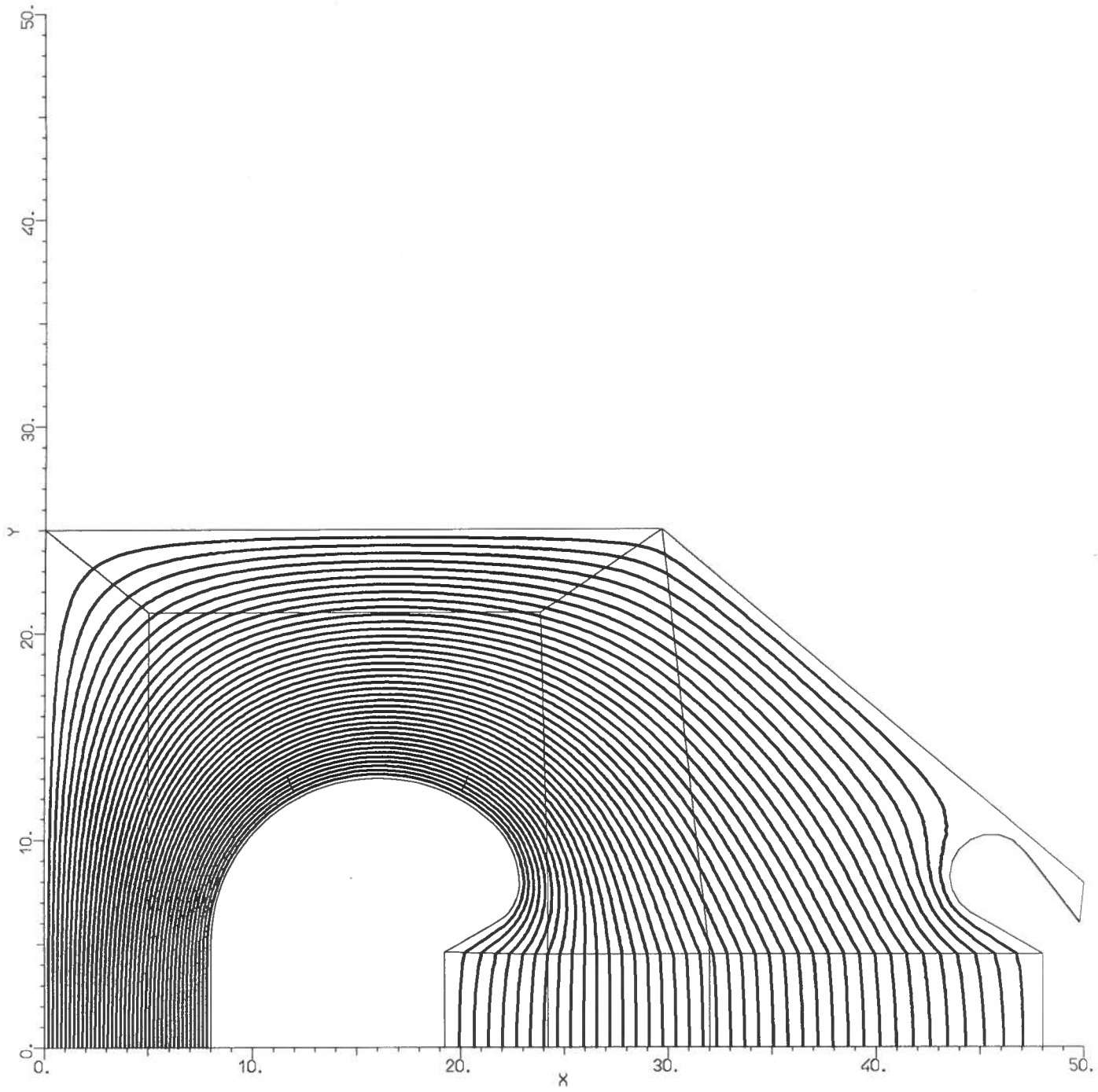

Figure 6.6.2: equipotential lines (step 2.5% of the applied voltage) for the insulator fixing zone (geometry I1), cartesian symmetry.

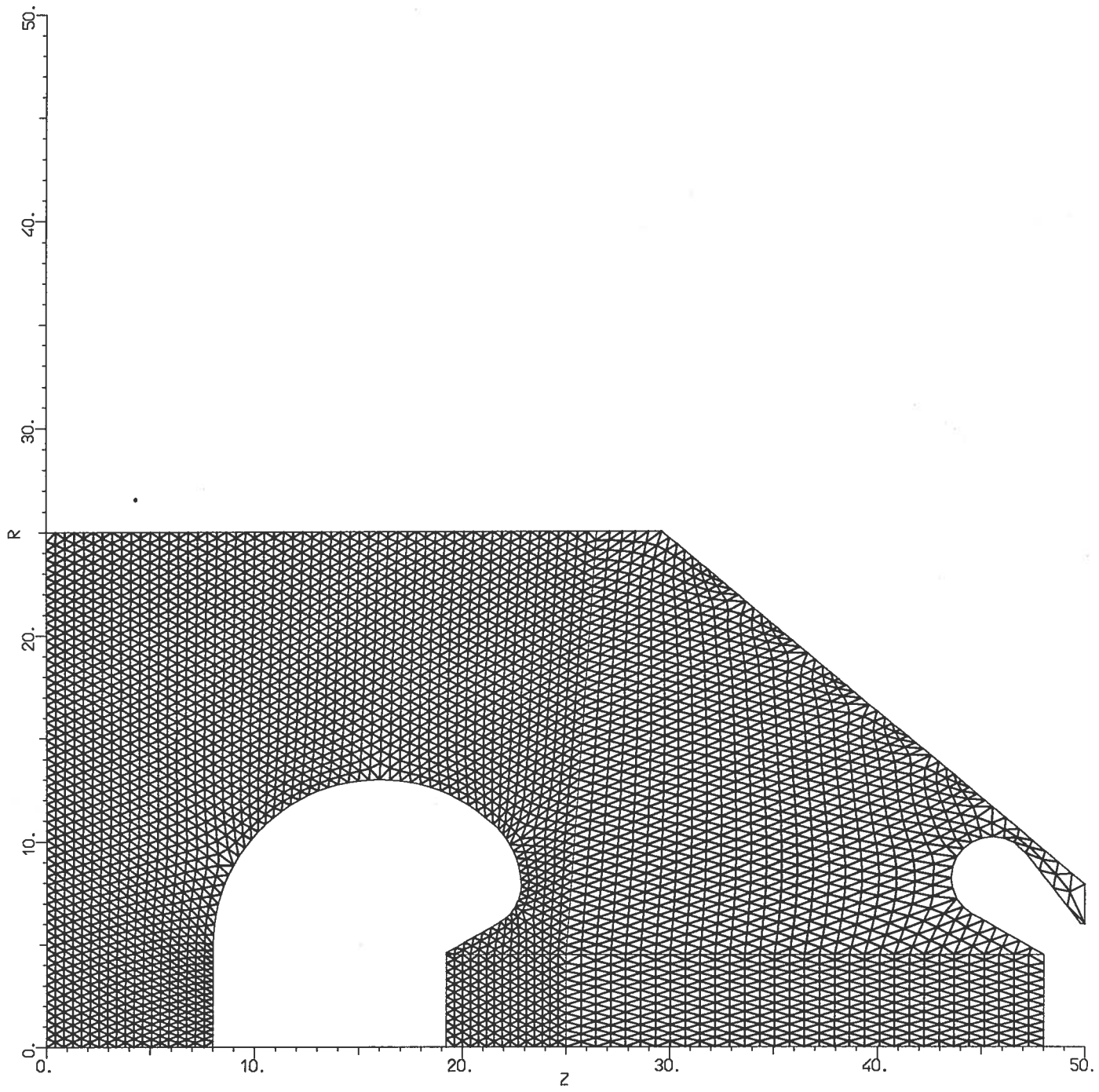

Figure 6.6.3: physical mesh for the insulator fixing zone (geometry I1), cylindrical symmetry.

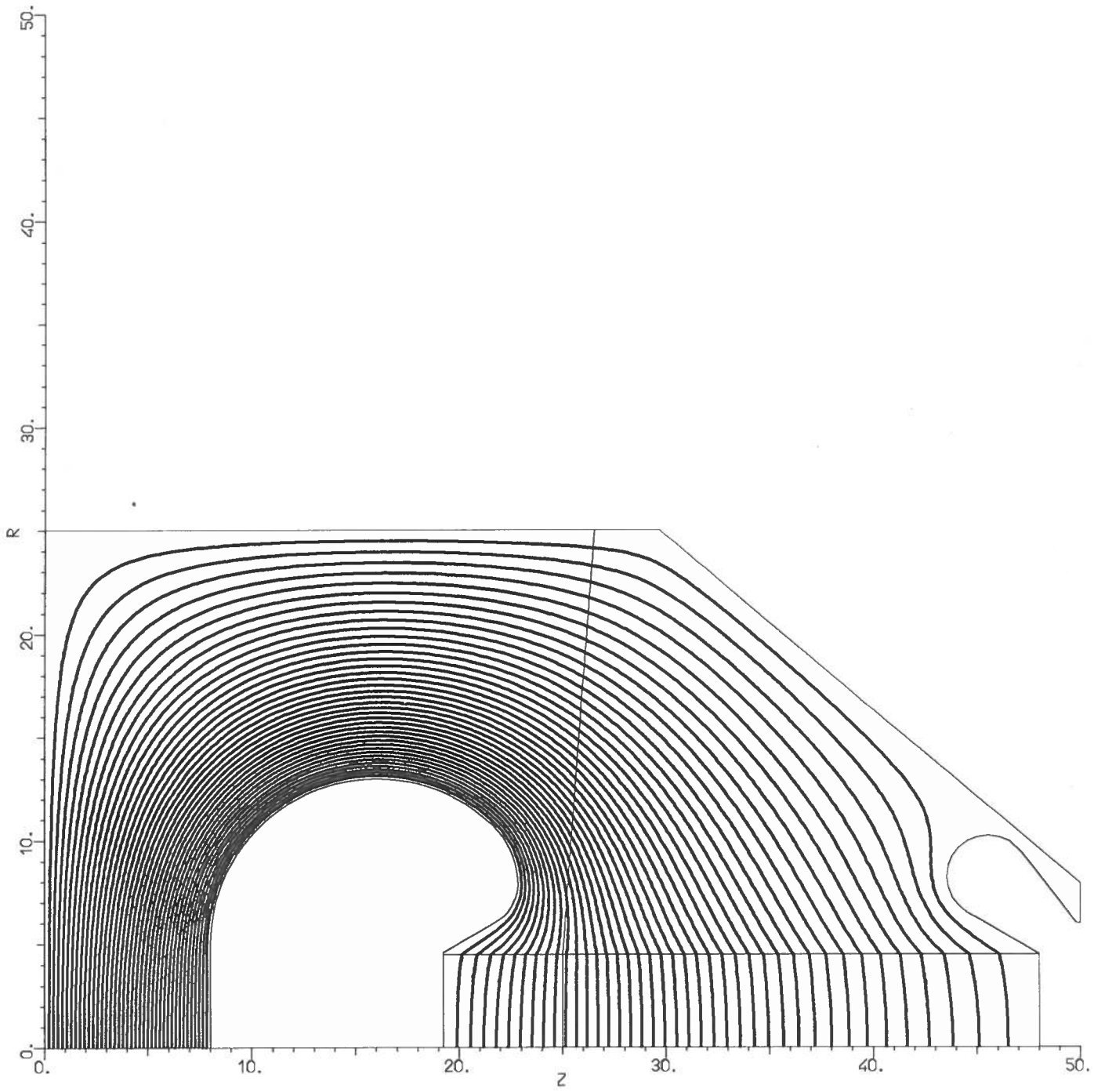

Figure 6.6.4: equipotential lines (step 2.5% of the applied voltage) for the insulator fixing zone (geometry I1), cylindrical symmetry.

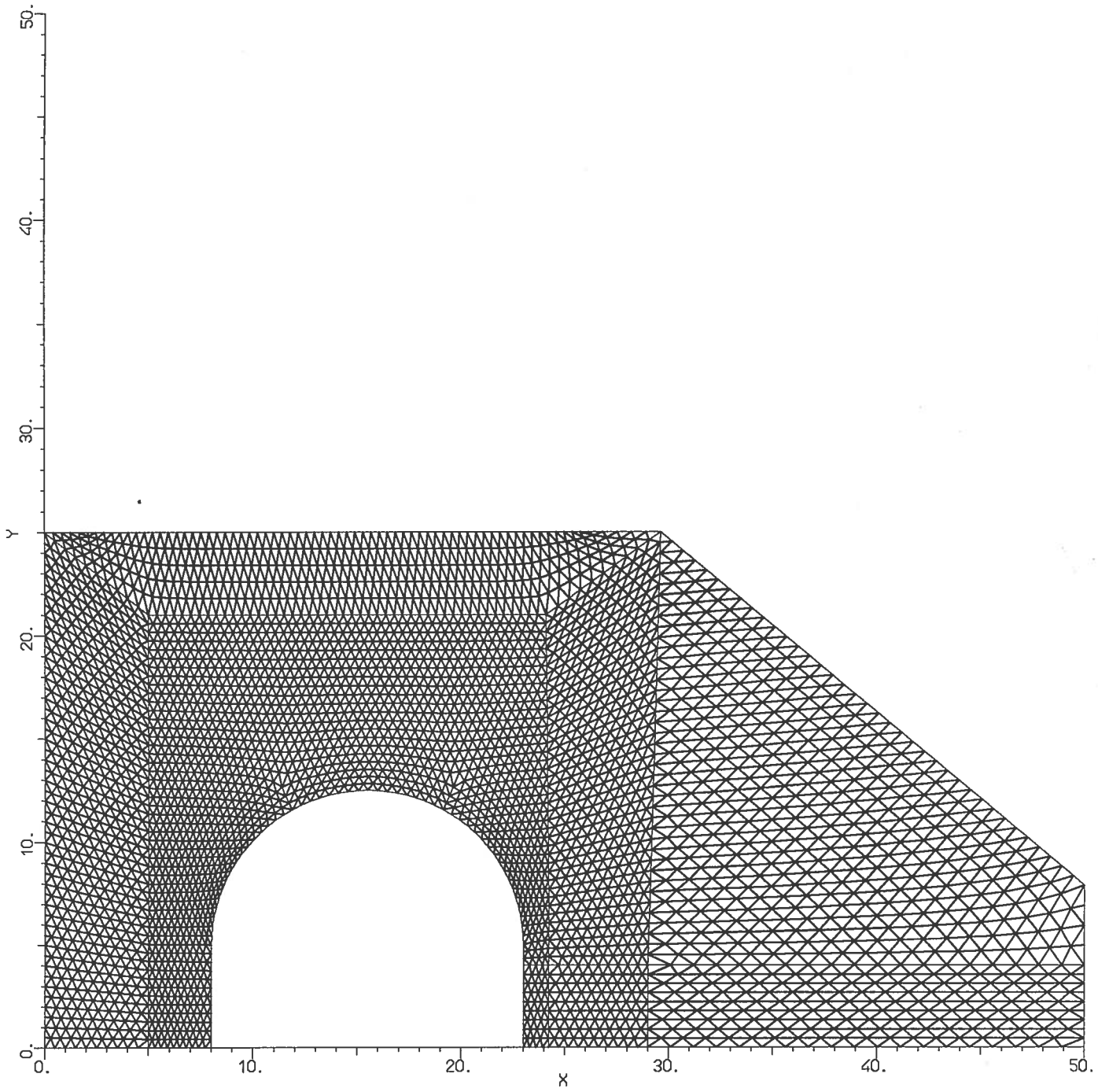

Figure 6.7.1: physical mesh for the insulator fixing zone (geometry I2), cartesian symmetry.

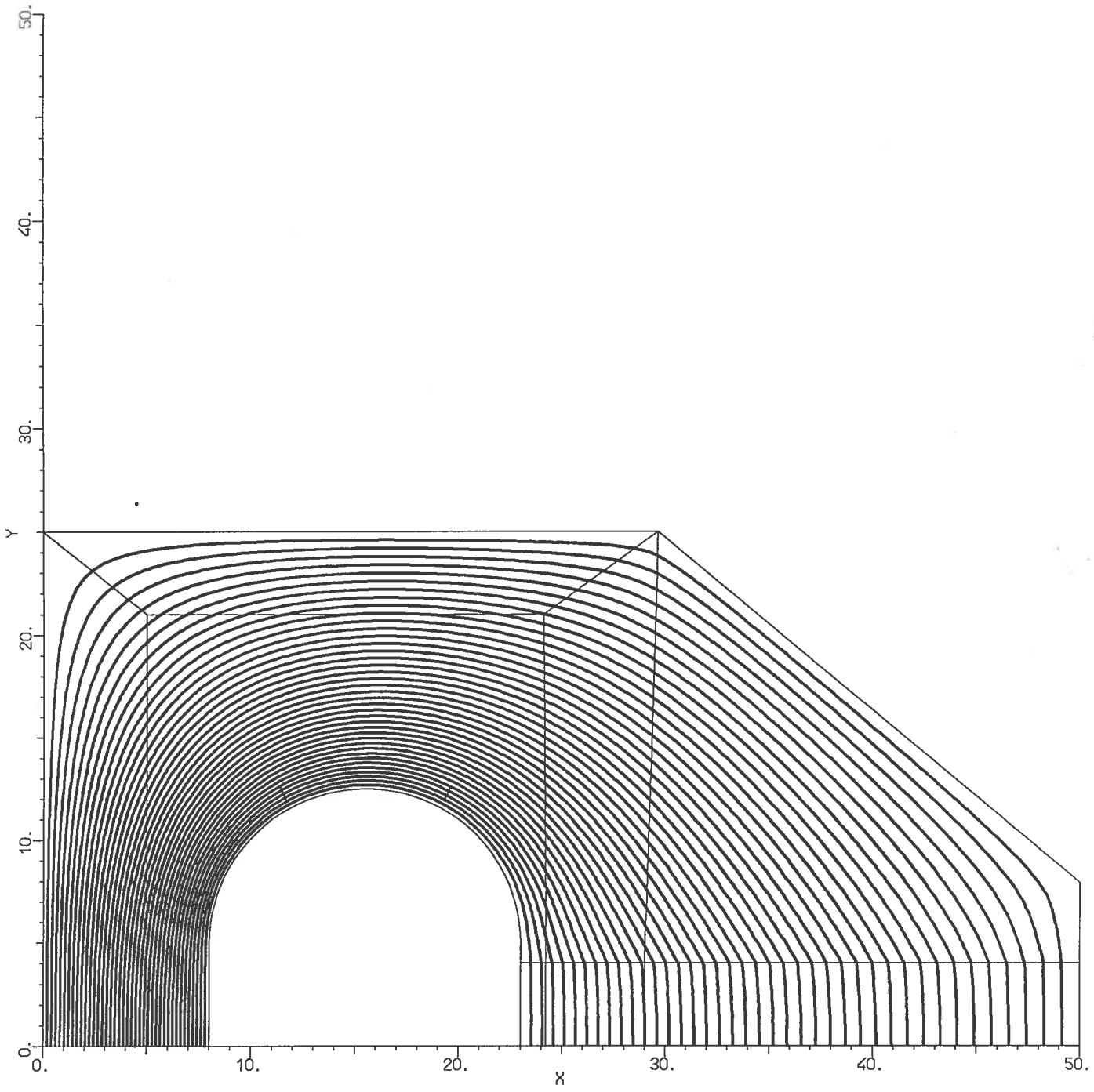

Figure 6.7.2: equipotential lines (step 2.5% of the applied voltage) for the insulator fixing zone (geometry I2), cartesian symmetry.

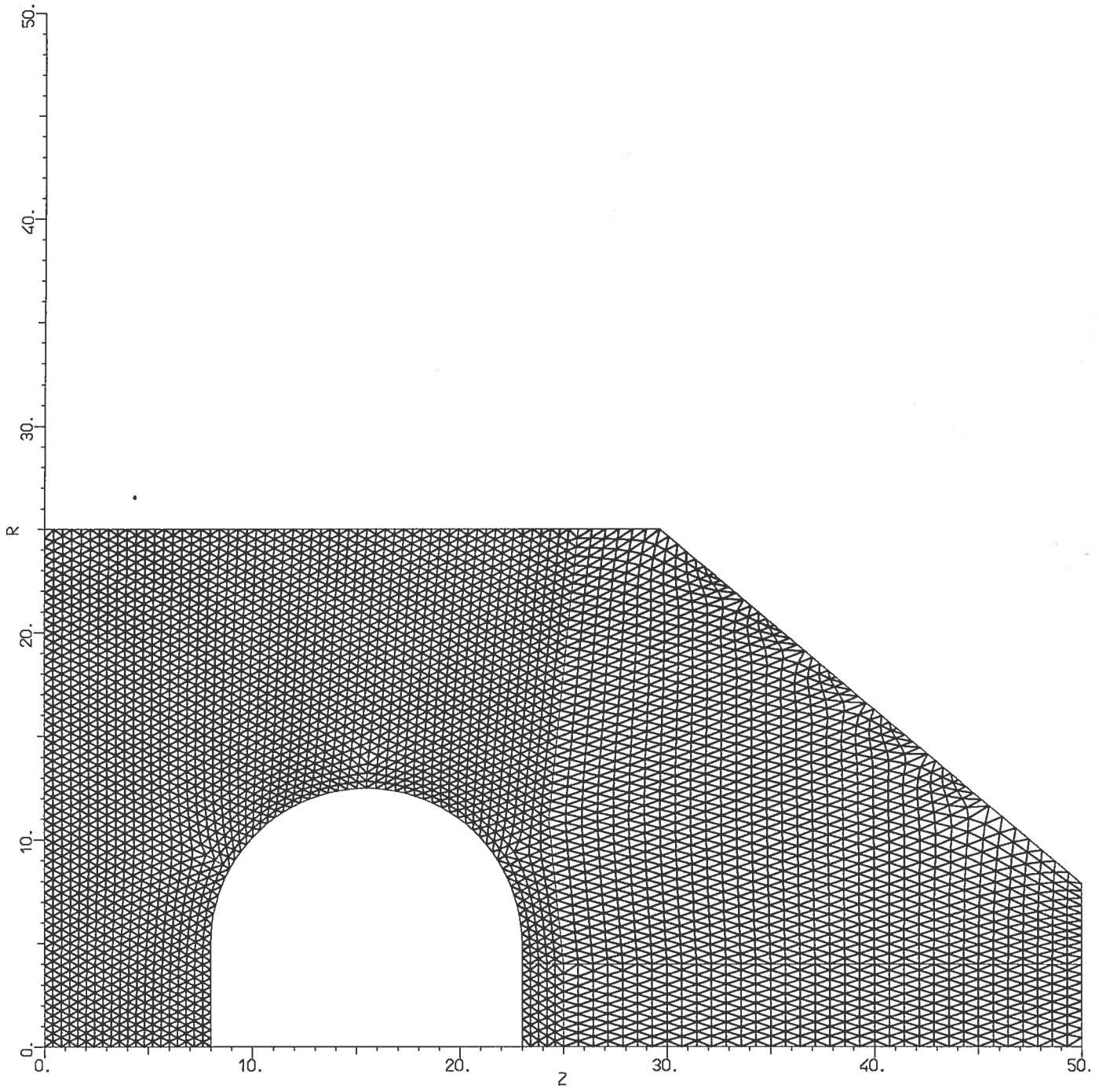

Figure 6.7.3: physical mesh for the insulator fixing zone (geometry I2), cylindrical symmetry.